

Systematic design and realization of double-negative acoustic metamaterials by topology optimization

Hao-Wen Dong^{1,2†}, Sheng-Dong Zhao^{3†}, Peijun Wei¹, Li Cheng², Yue-Sheng Wang^{4,5*}, Chuanzeng Zhang⁶,

¹*Department of Applied Mechanics, University of Science and Technology Beijing, Beijing 100083, PR China*

²*Department of Mechanical Engineering, The Hong Kong Polytechnic University, Hung Hom, Kowloon, Hong Kong, PR China*

³*School of Mathematics and Statistics, Qingdao University, Qingdao 266071, PR China*

⁴*Department of Mechanics, School of Mechanical Engineering, Tianjin University, Tianjin 300350, PR China*

⁵*Department of Mechanics, Beijing Jiaotong University, Beijing 100044, PR China*

⁶*Department of Civil Engineering, University of Siegen, D-57068 Siegen, Germany*

Highlights:

- Unified topology optimization framework is developed for designing double-negative acoustic metamaterials (AMMs).
- Representative resonance-cavity-based and space-coiling microstructures are explored.
- Broadband double negativity originating from novel multipolar LC (inductor-capacitor circuit) or Mie resonances can be induced by easily controlling optimization parameters.
- Desired broadband subwavelength imaging of topology-optimized AMMs is verified experimentally.

Abstract:

Double-negative acoustic metamaterials (AMMs) offer the promising ability of superlensing for applications in ultrasonography, biomedical sensing and nondestructive evaluation. However, the systematic design and realization of broadband double-negative AMMs are still missing, which hinder their practical implementations. In this paper, under the simultaneous increasing or non-increasing mechanisms, we develop a unified topology optimization framework involving different microstructure symmetries, minimal structural feature sizes and dispersion extents of effective parameters. The optimization framework is applied to conceive the heuristic resonance-cavity-based and space-coiling metamaterials with broadband double negativity. Meanwhile, we demonstrate the essences of double negativity derived from the novel artificial multipolar LC (inductor-capacitor circuit) and Mie resonances which can be induced by controlling mechanisms in optimization. Furthermore, abundant numerical simulations validate the corresponding double negativity, negative refraction, enhancement of evanescent waves and subwavelength imaging. Finally, we experimentally show the desired broadband subwavelength imaging by using the 3D-printed optimized space-coiling metamaterial. The present design methodology provides an ideal approach for constructing the constituent “atoms” of metamaterials according to any artificial physical and structural requirements. In addition, the optimized broadband AMMs and superlens lay the structural foundations of subwavelength imaging technology.

Keywords:

Acoustic metamaterial; Topology optimization; Double negativity; LC resonance; Mie resonance

[†] These authors contributed equally to this work.

* Corresponding author: yswang@tju.edu.cn

1. Introduction

Due to the fantastic wave characteristics, metamaterials [1-6] designed by engineering the subwavelength microstructures offer novel and exceptional opportunities for manipulating and controlling wave propagation, revealing the broad application prospects in various fields such as mechanics, materials, optics, electromagnetism, acoustics, and thermotics, etc. In general, conventional materials drive their wave motions from the properties of intrinsic atoms or molecules; metamaterials provide novel possibilities for constructing artificial “meta-atoms” (microstructures) with special geometry, physical features and spatial arrangements, thus bringing out many new functionalities. Electromagnetic metamaterials and metadevices can achieve a wide range of exotic electromagnetic responses, including negative refractive index, zero refractive index, optical chirality, anisotropy and hyperbolicity. Inspired by the optical metamaterials, acoustic metamaterials (AMMs) [2, 7], elastic metamaterials [8-12], mechanical metamaterials [5] and even graphene metamaterials [13] have been developed in many ways. Like other types of metamaterials, creating suitable building blocks of microstructures is the most fundamental and pivotal point for AMMs which exhibit diverse combinations of effective constitutive parameters—the mass density ρ_{eff} and bulk modulus K_{eff} . In the quadrants of AMMs, reported representative cases are single negativity ($\rho_{\text{eff}} < 0, K_{\text{eff}} > 0$; $\rho_{\text{eff}} > 0, K_{\text{eff}} < 0$), double negativity ($\rho_{\text{eff}} < 0, K_{\text{eff}} < 0$), double positivity ($\rho_{\text{eff}} > 0, K_{\text{eff}} > 0$) near-zero mass density ($\rho_{\text{eff}} \approx 0$), and even double-zero index ($\rho_{\text{eff}} \approx 0, 1/K_{\text{eff}} \approx 0$). Benefitting from the exotic effective properties, AMMs offer great potential for applications in low-frequency isolation, space sound field modulating, energy harvesting, perfect absorption, negative refraction, cloaking and nonreciprocal acoustic devices, and thus attracting the widespread and continuous attention during the past two decades. In acoustics, one of the most promising functionalities of AMMs is the subwavelength superlensing, warranting high-resolution ultrasonic imaging for medicine and industry [14-15]. Although the anamorphic effective refractive index [16] or phase difference [17] can enable the gradient metamaterials to focus waves in a focal plane, the conspicuous shortcoming is that their imaging resolutions cannot essentially break the diffraction limit. Alternatively, several strategies using microstructures [18-21] with different features of effective parameters can collect and exploit the evanescent wave field for the subwavelength details. One prominent technique for subwavelength imaging is the double-negative superlens [20]. It can cause the negative refraction, and then bring the diverging waves to reconvene and amplify the evanescent waves in the near field. Another approach relies on the anisotropic metamaterials [18-19] which can convert the coupling of near-fields emitted by subwavelength objects into propagating waves. In addition to the above strategies, time-reversal technique can also control and focus the subwavelength waves. By virtue of the Helmholtz resonators, the temporal response is recorded, flipped in time and radiated back, achieving the subwavelength focusing [21]. Furthermore, recent research indicates that, for metamaterials having relatively high index within a slow medium, the excitation of guided acoustic modes can transmit only subwavelength information to generate the subwavelength edge-based imaging [22]. In consideration of the operating bandwidth, in particular, the double-negative and hyperbolic metamaterials are more suitable for the broadband acoustic subwavelength focusing and imaging applications. In most cases, the hyperbolic metamaterials are highly desirable for the structure design. Only the three-dimensional membrane-type metamaterials [23] or layers of perforated plates [24] can produce the extremely anisotropic dispersion relations at the subwavelength scale. Nevertheless, double-negative metamaterials allow three choices including the coupled filter-element [25], coupled-membrane [26] and space-coiling structures [7]. Therefore, it is necessary to go into constructing the double negativity and the corresponding subwavelength superlensing.

In principle, the acoustic double negativity implies the several building blocks or specific elements supporting multiple overlapping resonances. The first approach is combining two resonating structures, membranes and Helmholtz resonators, to guarantee that their symmetric eigenmodes occur in the same dispersive frequency range, such as the example given in [25] to obtain the double negativity from 240 to 450 Hz based on a periodic array of

interspaced membranes and side holes. Alternatively, coupled-membrane resonators can also lead to double negativity with monopolar and dipolar eigenmodes in the range of 520–830 Hz [26]. In addition, the combination of clamped membranes and side branches can generate both anisotropic and double-negative properties as well [27]. It is found that detuned Helmholtz resonators with optimized coupling can also give rise to double-negative bands [28]. Moreover, the double negativity can be obtained through cavities drilled in the waveguide which contains the Helmholtz resonators for negative bulk modulus and a structured shell for negative mass density [29]. Another strategy, based on the ultra-slow Mie resonators consisting of macroporous microbeads [30], can also generate the negative acoustic index. Moreover, by coiling up space, the labyrinthine structures composed of hard solid plates inserted into the background fluid can cause the large phase delay and form the band folding in the low frequency range [7], thus exhibiting a frequency dispersive spectrum of a large refractive index not found in nature and double negativity without the traditional resonant elements. While the aforementioned methods preliminarily realized double negativity, the following problems and challenges need to be solved to achieve broadband double negativity for the subwavelength imaging. Firstly, from the perspective of microstructure design, the primary double-negative AMMs mainly depend on membranes or space-coiling structures. Compared with the membrane-type metamaterials, the space-coiling structures have attracted more attention for its strong control over the effective parameters and easy implementation. Because of the difficulties in constructing the pertinent zigzag path, however, most research only focus on the flexible phase manipulation [31] instead of the broadband double negativity within the spectrum of interest. Meanwhile, apart from the space-coiling metamaterials, designing various types of double-negative solid-air AMMs becomes a pressing issue to offer more choices for practical imaging applications. Secondly, regarding double-negative mechanism, existing AMMs mainly utilize the LC (inductor-capacitor circuit) resonance [25] induced from different resonant elements or the Mie resonance [30] produced by the particles with high refractive index relative to the background medium. There are, however, few works about the LC-resonance double negativity based on the artificial structures without membranes. Mie-resonance double negativity in a broadband range also challenges the microstructure design. Thirdly, with respect to the double-negative bandwidth, resonance-based AMMs usually suffer from frequency dispersions and narrow bands. Hence, it is imperative to broaden the frequency range of double-negative AMMs for solidifying their roles in diverse applications [32]. But in general, the above three issues are collectively limited by the manual and empirical design strategy.

With the advent of the burgeoning 3D printing technology, topology optimization has successively applied to the design of metamaterials to achieve the desired performance [11-12, 33-38]. Since AMMs have shown the unprecedented functionalities on wave manipulations, several topology optimization studies of AMMs were subsequently reported in recent years [35, 39-40]. However, these works mainly focused on the optimization of propagation responses [35] or positive wave parameters [39]. Furthermore, the topology-optimized AMMs only realized the expected narrow-band single negativity [40], anisotropic dispersion relation [35] and negative refraction [35], but lacking of the demonstration for subwavelength imaging. So topology optimization of AMMs is still in its infancy stage, although the increasing demand for more newfangled phenomena and acoustic devices is clearly foreseeable. Up to now, the inverse design of double-negative AMMs for airborne sound is still lacking, let alone the systematic optimization study. Moreover, unlike elastic metamaterials [8-12, 41], the negative effective parameters not only depend on the LC resonance, but also are possibly dominated by the Mie resonance. Because of the uncertain mechanism for negativity, topology optimization of double-negative AMMs is full of challenges.

In this paper, to provide a comprehensive guidance on engineering the double-negative AMMs, we show for the first time that the broadband double-negative AMMs can be systematically designed through topology optimization. A unified topology optimization framework is constructed for obtaining the broadband double negativity within the prescribed low frequency range. The proposed framework considers several typical structural

and physical characteristics of the microstructure, including unit-cell's symmetry (i.e., the square, chiral and orthogonal symmetries), minimal geometrical size (i.e., minimal size of the solid parts and the width of the air channels), variation trend and frequency dispersion of effective parameters. Band structures and retrieval of effective parameters demonstrate that the topology-optimized microstructures really exhibit the broadband double negativity. All metamaterials present here uncover two kinds of topological characteristics, i.e., the resonance-cavity-based and space-coiling layouts. Eigenstate analyses reveal that the optimization methodology under simultaneous increasing tendencies of the effective mass density and bulk modulus can give rise to the LC-resonance double negativity; whereas the simultaneous non-increasing tendencies can evoke the Mie-resonance double negativity. Then, the subwavelength negative refraction and acoustic imaging are numerically demonstrated after validating the equi-frequency surfaces and enhanced transmission of the evanescent waves. Finally, we fabricate a topology-optimized space-coiling AMM through 3D printing to successfully perform the subwavelength imaging in an acoustic experiment.

2. Topology optimization methodology

Consider the square-latticed microstructures consisting of solid and air elements for the acoustic wave propagation, as shown in Fig. 1. Based on the simulation model depicted in Fig. 1(a), the transmission and reflection coefficients of one microstructure can be calculated for the acoustic effective parameters retrieval, as long as the microstructure is symmetric along the direction of wave propagation. The dispersion relations of the microstructures can be characterized by the Floquet-Bloch theory. In topology optimization, the microstructure is divided into $N \times N$ pixels, in which air and solid are denoted by "0" and "1", respectively. It is assumed that the microstructure has three representative types of symmetries during topology optimization, i.e., square, chiral and orthogonal symmetries, as illustrated in Fig. 1(c). Because of this symmetry assumption, the design domain in the topology optimization changes from the whole unit-cell to a reduced space, see Fig. 1(c). Similarly, their corresponding irreducible Brillouin zones are displayed in Fig. 1(c).

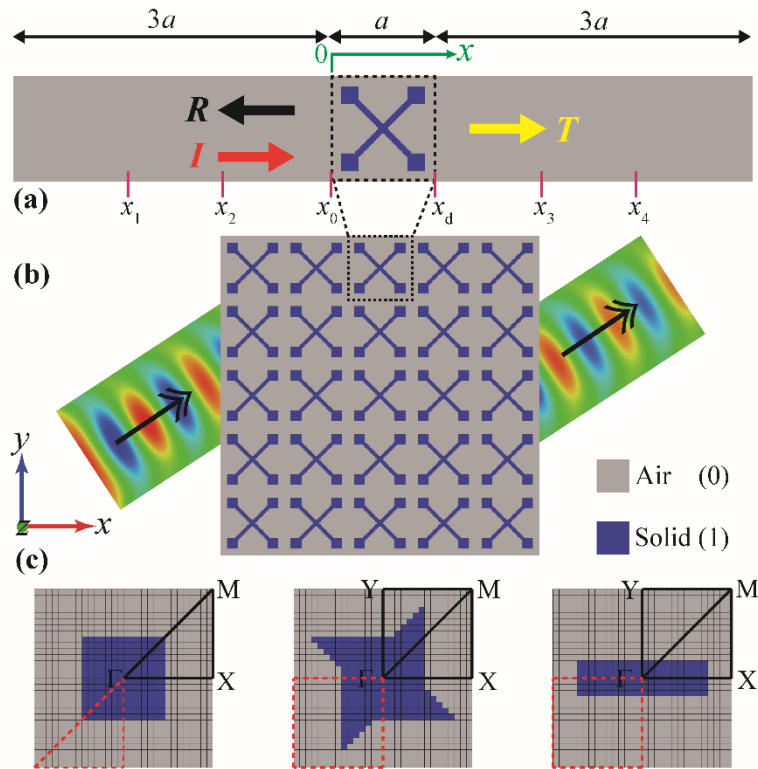


Fig. 1. Schematic illustration of the square-latticed AMMs and representative microstructural symmetries. (a) Wave propagation model for calculating the transmission and reflection coefficients of one microstructure. The simulation domain is terminated with the infinite elements at the left and right boundaries. The top and bottom edges are set as rigid walls. Four probes are introduced in the model for the scattering coefficients retrieval. (b) Double-negative AMMs with desired wave manipulation. (c) Three representative symmetries (left: square symmetry; middle: chiral symmetry; right: orthogonal symmetry) investigated in topology optimization. The dashed and solid lines show the corresponding reduced design domains and edges of the first reduced Brillouin zone, respectively.

2.1. Characterization of AMMs

To formulate the wave equations for the present high contrast (solid/air) wave problems shown in Fig. 1, the acoustic-structural interactions are ignored for simplicity. Because the solid can be regarded as perfectly hard, namely, the wave propagation is principally predominant in the background air [35, 42]; it is a good approximation to take the solid as a fluid with very high stiffness and specific mass [42]. Therefore, we only consider the traditional acoustic wave equation:

$$\nabla \cdot [\rho^{-1}(\mathbf{r})\nabla p(\mathbf{r})] + \omega^2 \lambda^{-1}(\mathbf{r})p(\mathbf{r}) = 0, \quad (1)$$

where p is the acoustic pressure; and λ for acoustic case equals to the bulk modulus K . According to the Floquet-Bloch theory, the acoustic pressure can be written as $p(\mathbf{r}) = e^{i\mathbf{k}\cdot\mathbf{r}}p_{\mathbf{k}}(\mathbf{r})$, where \mathbf{k} and $p_{\mathbf{k}}(\mathbf{r})$ are the Bloch wave vector of the first Brillouin zone and periodic function of \mathbf{r} , respectively. Considering the wave equation and boundary conditions, we can calculate the dispersion relation ($\omega-\mathbf{k}$) by using the ABAQUS/Standard solver Lanczos. Then the eigen-modes, phase velocity, group velocity and equi-frequency surfaces can be obtained from the band structures.

Under the long-wavelength assumption, a prominent trait of metamaterials is the feasibility of describing the artificial microstructure by the dynamic effective medium theory (EMT). For characterizing the AMMs, the primary and commonly used approach is extracting the acoustic effective properties from the reflection and transmission coefficients [43]. The essence of this inverse technique is reproducing the far-field scattering properties in an average sense through a uniform medium. To retrieve the effective constitutive parameters, the simulation model is regarded as a two-port network, shown in Fig. 1(a), in which an incident plane wave I propagates normally to the microstructure, with the reflection (R) and transmission (T) coefficients, respectively. Two probes are placed at x_1 and x_2 in the front and the other two at x_3 and x_4 in the back of the microstructure. After acquiring the total pressure of four probes, the four-microphone method [44] is adopted to calculate the scattering matrix \mathbf{S} of the microstructure, thus getting the effective refractive index and impedance. Finally, the effective mass density and bulk modulus can be further determined. For details, we refer to Ref. [43]. It is noted that the above four-microphone method is very easy to be implemented through the acoustic experiment.

In our simulation, the complex sound pressures at the four probes x_1, x_2, x_3 and x_4 are respectively expressed as

$$\begin{aligned} P_1 &= \left(A e^{ik_0 x_1} + B e^{-ik_0 x_1} \right) e^{-i\omega t}, \\ P_2 &= \left(A e^{ik_0 x_2} + B e^{-ik_0 x_2} \right) e^{-i\omega t}, \\ P_3 &= \left(C e^{ik_0 x_3} + D e^{-ik_0 x_3} \right) e^{-i\omega t}, \\ P_4 &= \left(C e^{ik_0 x_4} + D e^{-ik_0 x_4} \right) e^{-i\omega t}, \end{aligned} \quad (2)$$

where A, B, C and D denote the complex amplitudes of the positive- and negative-going plane waves; k_0 is the wave number in the background medium (air); ω is the circular frequency; $e^{-i\omega t}$ represents the common time-harmonic factor which is omitted throughout the paper for the sake of brevity; x_1, x_2, x_3 and x_4 denote the corresponding distances of four probes relative to respective reference planes in the two ports. Since the pressures

P_1, P_2, P_3 and P_4 can be directly obtained by the numerical simulation, the four coefficients A, B, C and D can be derived from Eq. (2) as

$$\begin{aligned} A &= -i \frac{P_1 e^{-ikx_2} - P_2 e^{-ikx_1}}{2 \sin(k_0 x_1 - k_0 x_2)}, \\ B &= -i \frac{P_2 e^{ikx_1} - P_1 e^{ikx_2}}{2 \sin(k_0 x_1 - k_0 x_2)}, \\ C &= i \frac{P_3 e^{-ikx_4} - P_4 e^{-ikx_3}}{2 \sin(k_0 x_4 - k_0 x_3)}, \\ D &= i \frac{P_4 e^{ikx_3} - P_3 e^{ikx_4}}{2 \sin(k_0 x_4 - k_0 x_3)}. \end{aligned} \quad (3)$$

The second order matrix relating the acoustic particle velocity and sound pressure on two faces of the microstructure in the simulation model shown in Fig. 1(a) is defined as the transfer matrix which is denoted as \mathbf{T} with the elements T_{ij} ($i, j=1, 2$). In view of the considered symmetries in Fig. 1(c), the effective two-port system [44] is reciprocal. In other words, \mathbf{T} should satisfy

$$T_{11} = T_{22}, \quad (4)$$

$$T_{11} T_{22} - T_{12} T_{21} = 1, \quad (5)$$

In addition, the simulation model has the following boundary conditions

$$p_0 = A + B, \quad (6)$$

$$p_d = C + D, \quad (7)$$

$$v_0 = (A - B) / Z_0, \quad (8)$$

$$v_d = (D - C) / Z_0, \quad (9)$$

where p_0 and p_d are the pressures at locations x_0 and x_d in Fig. 1(a), respectively; v_0 and v_d express the particle velocities at locations x_0 and x_d in Fig. 1(a), respectively; Z_0 is the impedance of the background medium. Then the transfer matrix of the effective two-port network can be written as

$$\mathbf{T} = \begin{bmatrix} T_{11} & T_{12} \\ T_{21} & T_{22} \end{bmatrix} = \begin{bmatrix} \frac{p_d v_d + p_0 v_0}{p_0 v_d + p_d v_0} & \frac{p_0^2 - p_d^2}{p_0 v_d + p_d v_0} \\ \frac{v_0^2 - v_d^2}{p_0 v_d + p_d v_0} & \frac{p_d v_d + p_0 v_0}{p_0 v_d + p_d v_0} \end{bmatrix}. \quad (10)$$

Based on the transformation relation between the scattering and transfer matrices [44], the scattering matrix can be obtained as

$$\mathbf{S} = \begin{bmatrix} S_{11} & S_{12} \\ S_{21} & S_{22} \end{bmatrix} = \begin{bmatrix} \frac{T_{11} + T_{12}/Z_0 - T_{21}Z_0 - T_{22}}{T_{11} + T_{12}/Z_0 + T_{21}Z_0 + T_{22}} & \frac{2(-T_{21}T_{12} + T_{11}T_{22})}{T_{11} + T_{12}/Z_0 + T_{21}Z_0 + T_{22}} \\ 2 & -T_{11} + T_{12}/Z_0 - T_{21}Z_0 + T_{22} \\ T_{11} + T_{12}/Z_0 + T_{21}Z_0 + T_{22} & T_{11} + T_{12}/Z_0 + T_{21}Z_0 + T_{22} \end{bmatrix}, \quad (11)$$

where S_{11} and S_{21} are the reflection R and transmission coefficient T , respectively. If the size of the microstructure is much smaller than the operating wavelength of the background medium (i.e., $\lambda_{\text{bk}} \geq 5a$), the composite microstructure can be regarded as the homogeneous medium [45-46], thus the effective impedance Z_{eff} and effective refractive index n_{eff} can be retrieved using the inverse technique [43] as

$$Z_{\text{eff}} = \frac{\eta}{1 - 2R + R^2 - T^2}, \quad (12)$$

$$n_{\text{eff}} = \frac{-i \ln \xi + 2\pi m}{k_0 a}, \quad (13)$$

where m represents the branch number of function $\cos^{-1}[(1-R^2+T^2)/2T]$; η and ξ are defined by

$$\eta = \mp \sqrt{(R^2 - T^2 - 1)^2 - 4T^2}, \quad (14)$$

$$\xi = \frac{1 - R^2 + T^2 + \eta}{2T}. \quad (15)$$

For passive metamaterials, the physically meaningful natural feature is that the sign of η should be chosen such that $\text{Re}(Z_{\text{eff}})$ is positive. The calculation of n_{eff} shown in Eq. (13) is highly dependent on the value of m . For thick metamaterials, m should be carefully selected which usually takes a finite value as integer. For the sake of simplicity, the metamaterial can be constructed with a minimal thickness whose size is much smaller than the wavelength so that $m=0$ can be guaranteed.

After Z_{eff} and n_{eff} have been determined, the effective mass density ρ_{eff} and bulk modulus K_{eff} are computed by

$$\rho_{\text{eff}} = \rho_0 Z_{\text{eff}} n_{\text{eff}}, \quad (16)$$

$$K_{\text{eff}} = \rho_0 c_0^2 Z_{\text{eff}} / n_{\text{eff}}, \quad (17)$$

where ρ_0 and c_0 are the mass density and acoustic velocity of the background medium, respectively. Meanwhile, the effective phase change $\Delta\phi_{\text{eff}}$ across the metamaterial layer can be obtained by $\Delta\phi_{\text{eff}} = \omega a \rho_{\text{eff}} / Z_{\text{eff}}$.

2.2. Design problem formulation

To realize a broadband double-negative AMM without membrane units, we need to construct a microstructure for resolving two emblematic challenges: (1) different resonance symmetries, including monopole, dipole and even quadrupole, have to be exploited through one microstructure; and (2) ρ_{eff} and K_{eff} should have the same dispersion property as frequency increases. Fortunately, as a systematic mathematical method, topology optimization involves the optimization of material layout in a huge design space $2^{N \times N}$, providing limitless possibilities for the occurrence of multiple resonances based on a brand-new topology. In general, the microstructure only holds single negativity [47-48] or very narrow-band double negativity [7, 29] if the variation tendencies of ρ_{eff} and K_{eff} are inconsistent. Consequently, it is essential to control their holistic properties and then guarantee the coincident performance.

From the previous studies on AMMs [7, 47], we find that the metamaterial usually possesses a relatively large n_{eff} before generating the negative properties, no matter whether the metamaterial has single negativity [47] or narrow-band double negativity [7]. More specially, the labyrinth microstructure has been demonstrated to be capable of achieving a long path length which is equivalent to a large n_{eff} [7]. As a result, the metamaterial can realize the band folding in the low-frequency range, thus creating the double negativity. For other types of AMMs [47-48] with single negativity, the negative ρ_{eff} or K_{eff} requires a resonance to generate an infinite effective value. That is, ρ_{eff} will increase from a positive value to the negative infinity and then derive the negative values. However, K_{eff} will decrease from a positive value to the infinity. Hence, in pursuing double negativity, ρ_{eff} and K_{eff} generally have the noticeable increasing and decreasing trends, respectively. In such a situation, the relatively large ρ_{eff} and relative small K_{eff} will allow the microstructure to possess a large n_{eff} over the entire spectrum of interest. Although n_{eff} will show the obvious dispersion property, its value can keep the quasi-static feature in the ultra-low frequency range. Therefore, regardless of the resonance mechanism and structural topology, the common prerequisite condition for double negativity is getting the relatively large n_{eff} in the ultra-low frequency range. When large n_{eff} induces the suitable resonances, it is essential to avoid the single negative ρ_{eff} or K_{eff} by adjusting and controlling the dispersion extent of ρ_{eff} and K_{eff} . In other words, the optimization model must properly punish

the degree of variation for ρ_{eff} and K_{eff} over the whole concerned spectrum while improving n_{eff} at the same time. Finally, to achieve broadband double negativity along the x direction within the target frequency ranges, a consolidated optimization formulation considering the prescribed physical mechanisms of effective constitutive parameters and special structural feature sizes is proposed as follows.

$$\text{For: } \omega \in [\omega_{\min}, \omega_{\max}] \quad (18)$$

$$\text{Maximize: } OF = N_n + \frac{n_{\text{eff}}^{x+1} \times n_{\text{eff}}^{x+1}}{M} - \frac{\alpha}{M} \times \max_{\substack{i=1,2,\dots,M' \\ j=1,2,\dots,N'}} \left[\frac{\max(\rho_{\text{eff}}^{x+j})}{\min(\rho_{\text{eff}}^{x+i})}, \frac{\max(K_{\text{eff}}^{+,j})}{\min(K_{\text{eff}}^{+,j})} \right], \quad (19)$$

$$\text{Subject to: } \rho_i = 0 \text{ or } 1 \ (i = N \times N), \quad (20)$$

$$CD_{\text{air}} = 1, \quad (21)$$

$$\min_{\Sigma} (w_a) \geq w_a^*, \quad (22)$$

$$\min_{\Sigma} (w_s) \geq w_s^*, \quad (23)$$

$$\beta = \begin{cases} \beta_1 = \min_{i=1,2,\dots,M'} [\rho_{\text{eff}}^{x+2} - \rho_{\text{eff}}^{x+1}, \dots, \rho_{\text{eff}}^{x+j} - \rho_{\text{eff}}^{x+j-1}] > 0 \\ \beta_2 = \min_{j=1,2,\dots,N'} [K_{\text{eff}}^{+,2} - K_{\text{eff}}^{+,1}, \dots, K_{\text{eff}}^{+,j} - K_{\text{eff}}^{+,j-1}] > 0 \end{cases} \quad (\text{case 1}), \quad (24)$$

$$\beta = \begin{cases} \beta_1 = \min_{i=1,2,\dots,M'} [\rho_{\text{eff}}^{x+2} - \rho_{\text{eff}}^{x+1}, \dots, \rho_{\text{eff}}^{x+j} - \rho_{\text{eff}}^{x+j-1}] \leq 0 \\ \beta_2 = \min_{j=1,2,\dots,N'} [K_{\text{eff}}^{+,2} - K_{\text{eff}}^{+,1}, \dots, K_{\text{eff}}^{+,j} - K_{\text{eff}}^{+,j-1}] \leq 0 \end{cases} \quad (\text{case 2}),$$

where ω_{\min} and ω_{\max} are the upper and lower bounds of the target frequency range which is divided by M sampling frequency points; OF denotes the objective function; N_n is the number of sampling frequency points where the double negativity is implemented; n_{eff}^{x+} , ρ_{eff}^{x+} and K_{eff}^{+} are the arrays of positive n_{eff}^x , positive ρ_{eff}^x and positive K_{eff} , respectively; M' and N' are the numbers of the elements which belong to the arrays of ρ_{eff}^{x+} and K_{eff}^{+} , respectively; n_{eff}^{x+1} denotes the first positive effective refractive index of an array of n_{eff}^{x+} ; α is a prescribed parameter for regulating the whole dispersion extents of ρ_{eff}^x and K_{eff} ; ρ_i represents the material phase in optimization and declares the air (0) or solid (1) attribute of a pixel; CD_{air} denotes the number of the connected air domains in the microstructure; Σ stands for the design domain shown in Fig. 1(c). Here we employ the simple geometrical constraint in Eq. (21) based on the fact that multiple connected air domains usually reduce the wave transmission and will form several closed cavities, resulting in extremely narrow bandwidths of the resonances. Note that two special structural constraints in Eqs. (22) and (23) are introduced to ensure meaningful microstructure from physics and manufacturing perspective, respectively. Given that the AMMs with very narrow air channels usually incur the significant viscous losses which are induced by the near-wall viscosity effect [47], it is necessary to restrict the dimensions of all air channels for circumventing this problem. More specifically, the minimum size of the array w_a composed by every air channel should be larger than a pre-set parameter w_a^* . Furthermore, similar control over the solid components is also needed for topology optimization, especially for satisfying the sufficient strength and fabrication requirement of the metamaterial samples [11-12, 47]. Therefore, we set the constraint in Eq. (23) to cope with these two issues, i.e., the minimum size of an array w_s including

every solid must be larger than an empirical value w_s^* .

Moreover, without taking particular control measure, inducing the overlapping resonances can easily bring about two different and inconsistent variations for ρ_{eff}^x and K_{eff} , thus jeopardizing the formation of broadband double negativity. Therefore, we use the special physical constraint in Eq. (24) to precisely control the variation of ρ_{eff}^x and K_{eff} at the sampling frequency points. In terms of the discrete positive ρ_{eff}^{x+} and K_{eff}^+ , their possible variation with the increase of frequency can be generalized into two major categories: one is the simultaneous increasing tendency (i.e., case 1); the other is the simultaneous non-increasing tendency (i.e., case 2). Throughout this paper, we will demonstrate the crucial role of these two mechanism constraints for inducing two novel double-negative microstructures.

Obviously, the optimization problem in Eqs. (18)-(24) involves different kinds of constraints, intensifying the difficulties of optimization search in a large design space. Many topology optimization methods can effectively solve the various structural optimization problems in different fields [49-52]. Here, owing to the strong versatility, the improved two-stage single-objective genetic algorithm (GA) [11-12, 53-54] is utilized to solve the proposed optimization problem. GA treats the microstructure in $N_1 \times N_1$ pixels as a binary chromosome and mimics the evolutionary process by applying the natural selection principle to every generation towards the best design solution. First, an initial population of N_p individuals is randomly generated. To improve the effectiveness of any microstructures, a special ‘‘abuttal entropy filtering’’ [54] is applied for every microstructure to slightly fill up some isolated voids and remove some isolated elements. Secondly, every individual is evaluated for the fitness function and constrains. Then, GA uses the repetitive operators including the tournament selection, uniformed-matrix crossover and uniformed-matrix mutation to produce the offspring generation. Finally, the representative elitism strategy [53] is utilized to improve and accelerate the optimization. After the prescribed number of generations, GA produces the optimized individual at the first stage. Introducing the optimized individual as the ‘‘seed’’ structure with $N_2 \times N_2$ pixels, GA are performed through the corresponding genetic operators at the second stage. Repeat all procedures generation by generation, and then bring about the final optimized microstructure towards to optimization problem in Eqs. (18)-(24).

3. Results and discussions

In this section, the proposed topology optimization formulation in Eqs. (18)-(24) is applied to design the square-latticed subwavelength metamaterial to obtain the broadband double negativity within a target frequency range $[\Omega_{\text{min}}, \Omega_{\text{max}}]$. Three representative symmetries including the square, chiral and orthogonal cases are investigated to give the synthetical and thorough insight into the beneficial topological feature of microstructures. All optimizations reported in this paper start from a random initial population. We adopt the following mass densities and speeds of sound for the air and solid materials: $\rho_{\text{air}}=1.204 \text{ kg/m}^3$, $c_{\text{air}}=343 \text{ m/s}$, $\rho_{\text{solid}}=1230 \text{ kg/m}^3$ and $c_{\text{solid}}=2230 \text{ m/s}$ [55]. In fact, our numerical tests indicate that the acoustic-structural interaction has only a negligible effect on the performance of the effective parameters in the subwavelength range for the cases investigated in this paper. In general, the effects of the acoustic-structural interaction may have a visible difference between the ‘‘harder’’ and ‘‘softer’’ solids. For the analyses of the optimization performance, unless otherwise stated, the target frequency range is defined as [100 Hz, 8000 Hz]. The normalized frequency $\Omega=\omega a/2\pi c$ is introduced for convenience, where a denotes the lattice constant, and c is the acoustic velocity of the air. The normalized target range is $[\Omega_{\text{min}}, \Omega_{\text{max}}]=[0.002476, 0.198061]$. The number of sampling frequency points M is set as 11, which is suggested by the numerical tests considering the computing cost and effectiveness of the discrete description. The

solid constrained parameter is selected as $w_s^* = a/30$ in all optimizations. The parameters of the GA are the population size $N_p=30$, the crossover probability $P_c=0.9$, the mutation probability $P_m=0.02$, and the championship selection size $N_c=18$. At the first stage, the optimization is performed by 2500 generations in 30×30 pixels. For the fine description of topologies, the optimization with other 2500 generations is executed in 60×60 pixels. Meanwhile, the optimized microstructure in the first stage is introduced as an initial configuration in the second stage. All two-stage optimization processes are implemented within 34.5 hours on a Linux cluster with Intel Xeon X5650 Core @ 2.66 GHz. The numerical simulations of dispersion relations, effective parameters, eigenstates, transmission spectra and evanescent wave transmission are carried out by ABAQUS 6.14-1. Simulations of negative refraction and acoustic subwavelength imaging are accomplished by COMSOL Multiphysics 4.4. An acoustic experiment is conducted to demonstrate the subwavelength imaging of topology-optimized space-coiling AMM to exhibit the correctness of explored double-negative mechanisms and then to show the potential of our topology optimization framework.

3.1. Optimized double-negative AMMs under simultaneous increasing tendencies of the effective parameters

This subsection presents the optimization results with the prescribed simultaneous increasing tendencies ($\beta > 0$) of the effective parameters, ρ_{eff}^x and K_{eff} (i.e., case 1 in Eq. (24)) for the normalized subwavelength target range [0.002476, 0.198061]. Some representative topological features, evolution history, various physical characterizations, negative properties of optimized metamaterials are analyzed and discussed in details. The typical and novel LC resonances contributing to the acoustic broadband double negativity are revealed through the resonance-cavity-based AMMs for the first time. All mentioned frequencies in the following contents refer to the normalized ones.

3.1.1. Topology-optimized resonance-cavity-based AMMs

3.1.1.1 Square, chiral and orthogonal symmetries

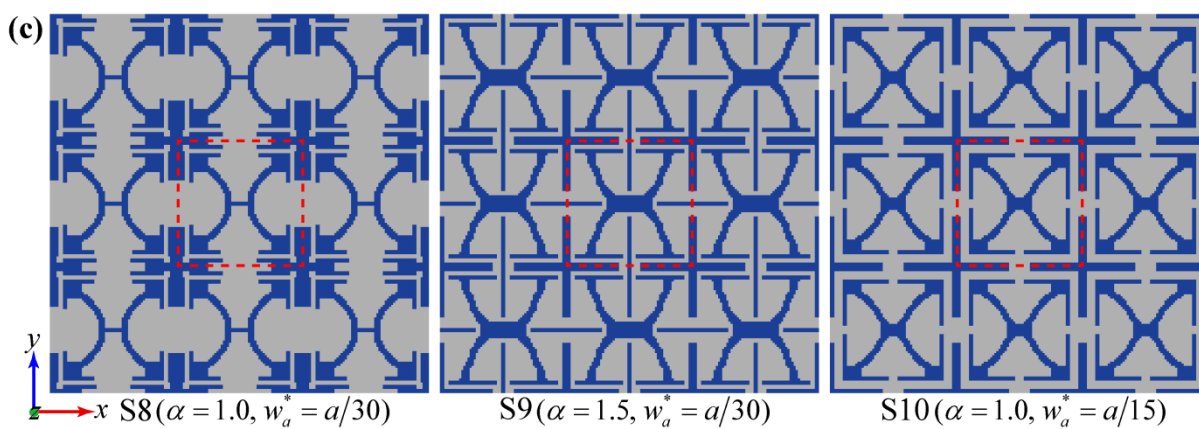
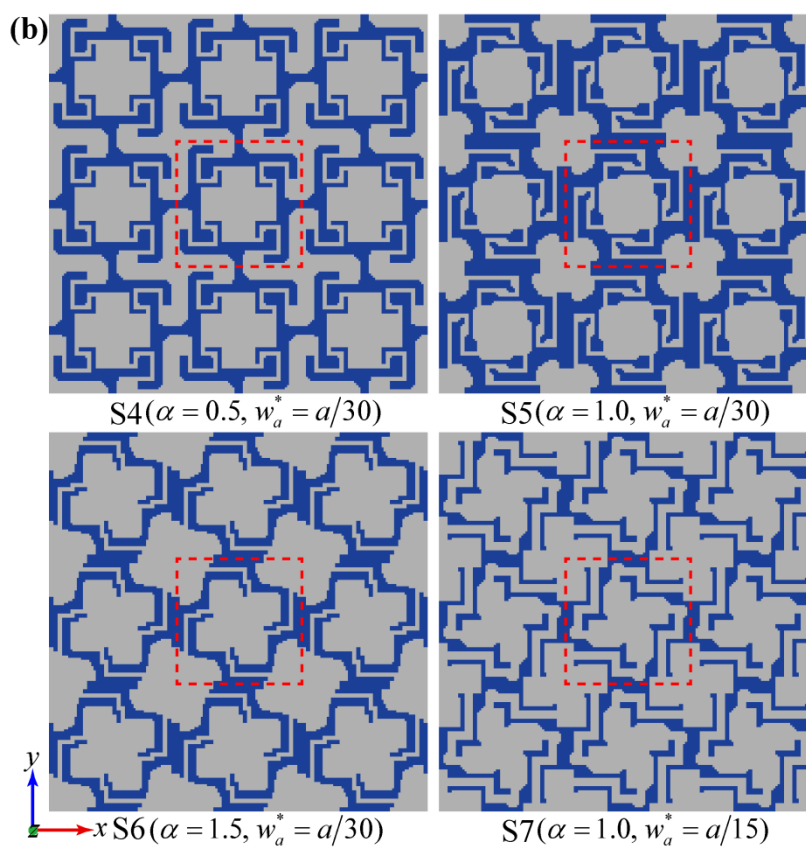
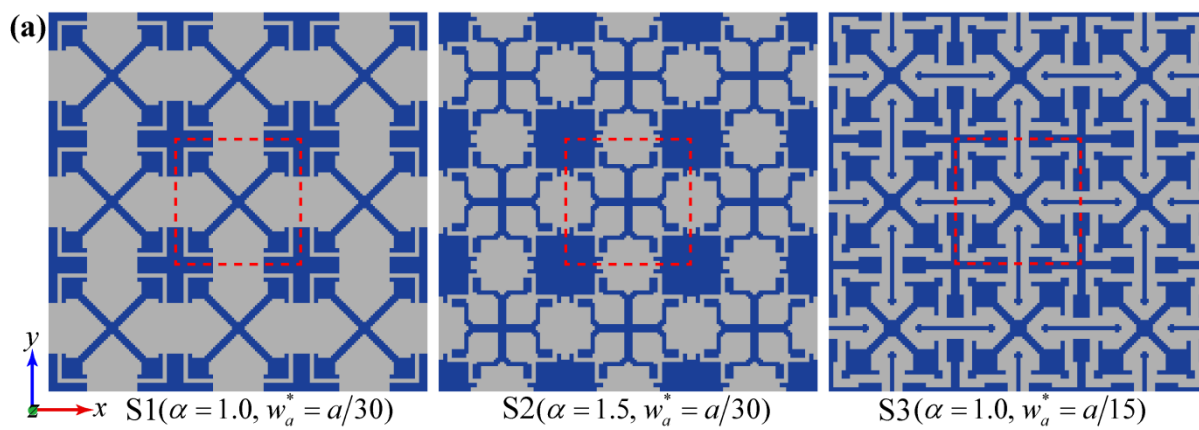
We firstly design the microstructure with square symmetry and explore the effects of α and air channel width on optimized topologies and double negativity, as shown in Fig. 2(a). Extracting their macroscopic geometry features, it is interesting to observe some common characteristics: (1) big air cavities connected through narrow air channels, and (2) big solid regions separated by the air domains. Like the Helmholtz resonator [2], multiple cavities in Fig. 2(a) can induce the negative effective bulk modulus. The distributions of hard solids can cause the large reflection with the limited space, which is beneficial for the occurrence of large refractive index. The above characteristics of resonance and large refractive index are dovetailed with the settings of the objective function in Eq. (19). With a larger α , the metamaterial S2 has more cavities than S1. For the air-solid metamaterials with the viscous losses [47], the widths of air channels have appreciable impact on the efficacy of metamaterials. Fortunately, increasing this feature size can admittedly reduce the viscosity factor of metamaterials. To show the effect of air channels, we illustrate the optimized metamaterial S3 for the typical feature sizes of $w_a^* = a/15$ in Fig. 2(a). Compared with S1, S3 has the similar topological features except four additional slender hard solid plates. For clearly showing the desired negative properties, we present in Fig. 2(d) the double-negative ranges and quasi-static refractive index and impedance of the AMMs in Fig. 2(a). Since the effect of α is non-monotonic, we can only suggest its suitable range of [1.0, 1.5] in which double negativity can be effectively realized. The

relatively larger refractive index usually enables a relatively wider double negativity. Combing the microstructure topologies, the variation of impedance shows that a reduction of air cavity domains can cause an increase of the impedance. Hence S1 can keep the relatively large refractive index while maintaining the reasonable wave transmission. The difference between S1 and S2 shows that the superabundant cavities may result in the narrow-band double negativity. The difference between S1 and S3 suggests that wider air channels will evoke smaller regions of air cavities, ultimately leading to a narrow-band double negativity.

To check the effectiveness of the proposed optimization formulation, we further investigate the topology optimization with chiral and orthotropic symmetries, see Figs. 2(b) and 2(c). Figure 2(d) displays their double-negative ranges and quasi-static refractive indices and impedances. All chiral metamaterials in Fig. 2(b) contain a large air cavity in the center and four rotationally distributive solid blocks. For the unit-cell domains marked by dashed lines, four corner regions of the metamaterial can be regarded as four small air cavities. With the same w_a^* , S5 has double negativity property than S4 and S6. So $\alpha=1.0$ is effective to balance the large refractive index and appropriate dispersion extent. Unlike the square-symmetry case in Fig. 2(a), the topology of S7 demonstrates that large w_a^* prescribed in optimization can naturally make the solid components thinner. Moreover, the chiral symmetry is superior to the square symmetry if the complexity of structure is ignored. The double-negative ranges of optimized chiral metamaterials are apparently larger than those of the square-symmetry ones in Fig. 2(a). Therefore, multiple air cavities combined with the zigzag air channels and solid parts provide the ideal geometrical platform for the broadband double negativity.

Figure 2(c) presents the optimized orthogonal-symmetry metamaterials. For the subwavelength imaging, it is essential to make sure that the effective bulk modulus is isotropic during optimization for all potential designs. Although the effective bulk modulus is normally isotropic if the operating wavelength is larger than $5a$ (recall that a is the lattice constant) [45-46], many highly complex orthogonal-symmetry metamaterials in optimization may have distinct behaviors along two principle directions, resulting in the high anisotropy and even possible coupling of effective bulk modulus using the present simulation model in Fig. 1(a). As a remedy approach, we force the relative difference between K_{eff} retrieved from the x and y directions to be smaller than 5%. We can observe from S8 and S9 that the multiple air cavities and several isolated solid blocks become the main topological features for double negativity. Similar with the results in Fig. 2(a), increasing α tends to increase the numbers of the air cavities and solid blocks. The difference between S8 and S10 shows that the geometry would be simpler and has the thinner hard solid plates when wider air channels are needed.

Through comparing the results in Fig. 2(d) for the three cases, we can make the following observations. For the low-frequency property, the optimized AMMs show good double negativity, with chiral symmetry being the best followed by orthogonal symmetry. The behaviors of refractive index and impedance are positively correlated. The orthogonal-symmetry AMMs can realize the similar refractive index with the chiral-symmetry ones. But the chiral-symmetry AMMs have to face the relatively large impedance. Comparing the double-negative ranges of S4-S7, we find that the effect of α is smaller than that of the minimal air channel width. Similar feature can be observed from the orthogonal-symmetry case. Therefore, the control over the feature size of the air channels should be a pivotal factor in designing the double-negative AMMs for practical applications. Given the same topological features, increasing the air channel widths will result in a decrease of the refractive index and impedance for the optimization under simultaneous increasing tendencies. For the chiral symmetry, the relatively large (1.5) or small (0.5) α will result in a smaller refractive index. However, for the orthogonal symmetry, larger α can lead to a larger refractive index for double negativity.



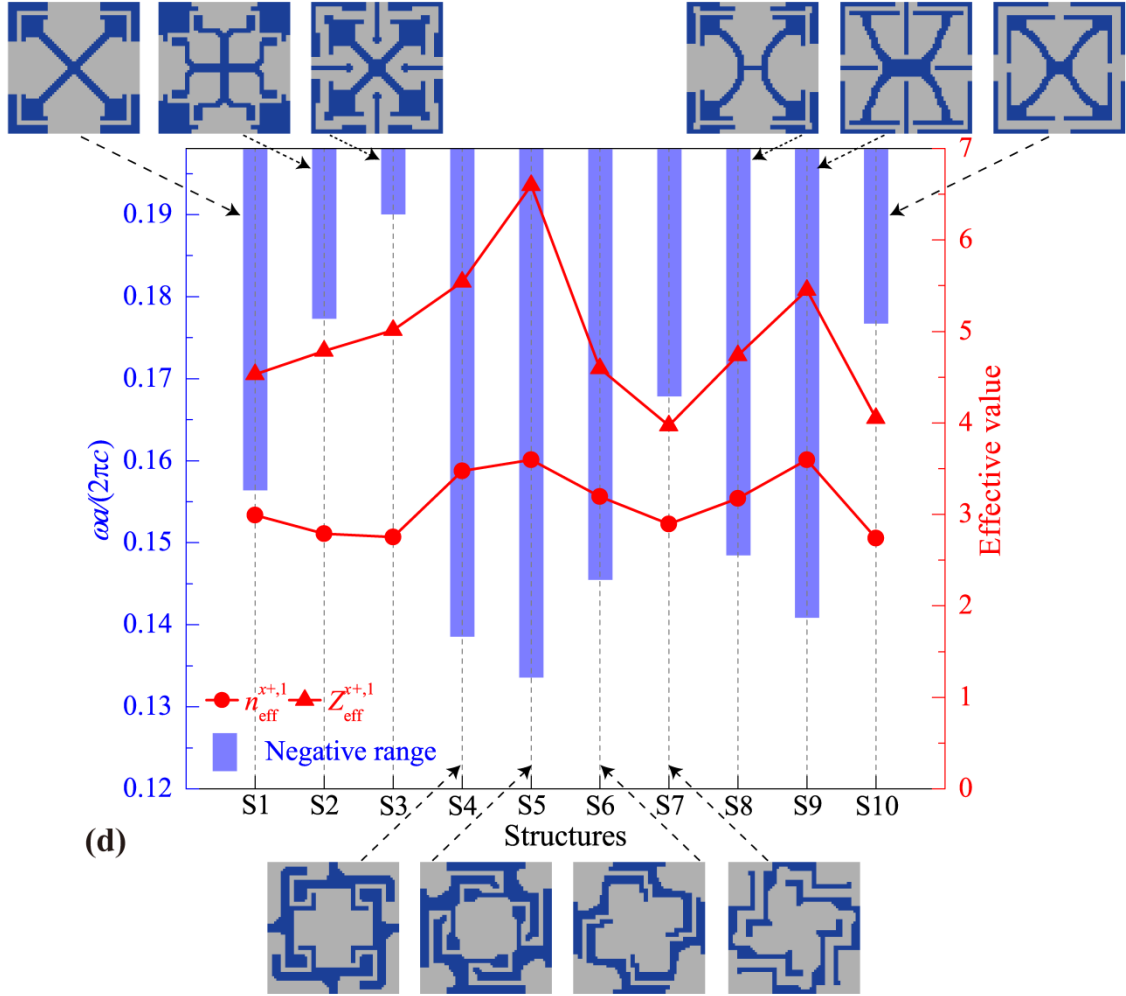


Fig. 2. Topology-optimized resonance-cavity-based AMMs with three representative symmetries. (a)-(c) Optimized metamaterials. All topology-optimized metamaterials are under the constraint of $\beta > 0$. The target spectrum of S1-S10 is selected as $[0.002476, 0.198061]$. For the microstructures S8-S10, to guarantee the isotropy of effective bulk modulus, the relative difference between K_{eff} retrieved from the x direction and y direction wave simulations are forced to be smaller than 5%. (d) Comparisons of the double-negative range, quasi-static effective refractive index n_{eff}^{x+1} and impedance Z_{eff}^{x+1} at Ω_{min} for S1-S10. More performances are summarized in Appendix A.

Based on the solid-air system, the present topology optimization can effectively realize the novel multi-cavities microstructures having ideal double negativity, and overcome the limitations of single negativity of the Helmholtz metamaterials [2, 25]. From the prospective of double negativity, introducing the chirality is the best design approach; followed by the orthogonal symmetry and the square symmetry. Similarly, the chiral symmetry can induce the largest refractive index. From the prospective of topological features, three symmetric AMMs share the common ground for double negativity: multiple air cavities, solid blocks and relatively narrow air channels.

3.1.1.2 Analysis of representative AMM S1

In view of the most concise topological features and satisfactory double negativity, the AMM S1 is suitable to be systematically analyzed as the representative metamaterial. To clarify the evolution for the optimized topology of S1 in Fig. 2, Figure 3 shows the evolutionary history of the maximal fitness with the generation number during

the “coarse to fine” optimization process. Topology optimization starts from a randomly generated microstructure ($G=0$), which cannot satisfy the particular constraints of Eqs. (21)-(24). From the generation $G=20$ ($F=0.1066$) to $G=215$ ($F=0.2563$), GA can quickly capture the beneficial topological feature during the early evolution stage, i.e., four air cavities and two solid blocks. The maximal fitness change between $G=215$ ($F=0.2563$) and $G=320$ ($F=2.6097$) implies that the small central solids can contribute to the formation of double negativity. From the generation $G=320$ ($F=2.6097$) to $G=3435$ ($F=3.7124$), the microstructure turns to possess the longer air channels at four corners between the air cavities. Furthermore, the microstructure obtains the clearer edge descriptions and more smooth geometrical layouts. From $G=3435$ ($F=3.7124$) to $G=4276$ ($F=3.7213$), the slightly increased fitness demonstrates that the larger cavities should be a better choice under the circumstance with unchanged air channels. Therefore, we can generalize the beneficial topological features for the square-symmetry AMMs: four large enough air cavities, two independent solid blocks, narrow enough air channels and several slender hard solid plates.

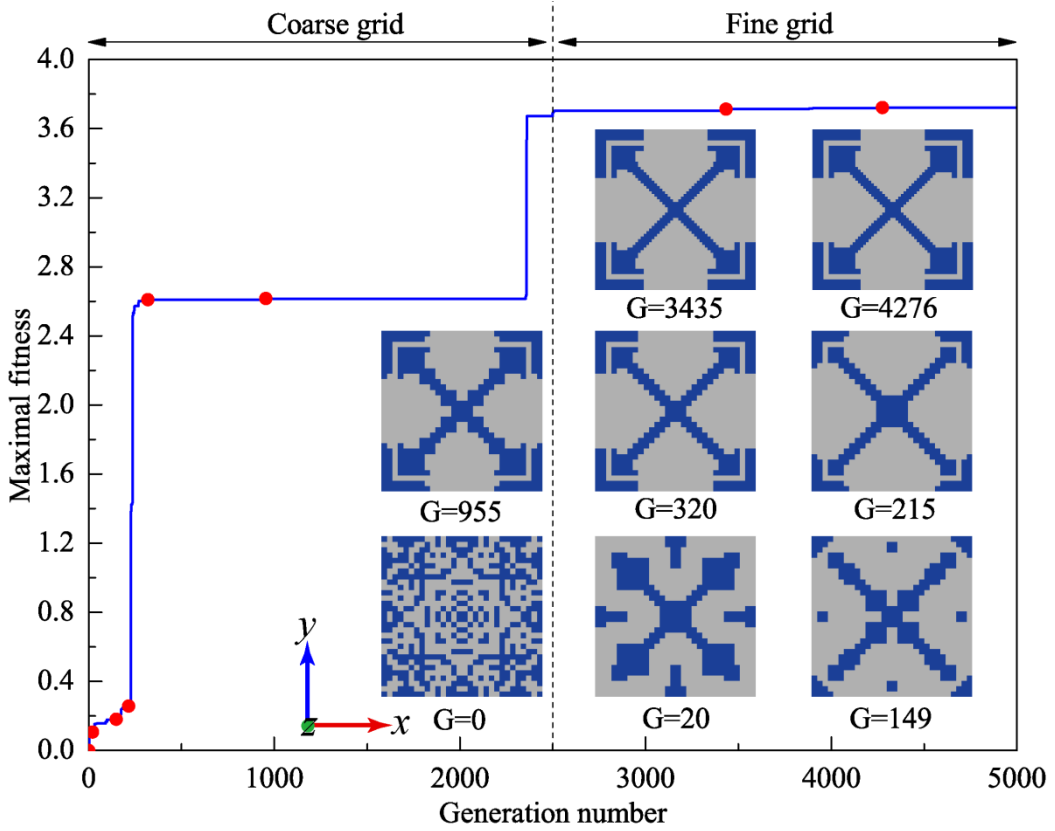


Fig. 3. Evolutionary history for the generation of topology-optimized AMM S1 in Fig. 2. Illustrations display eight representative topologies during the “coarse to fine” optimization. The objective function values of eight microstructures are 0 ($G=0$), 0.1066 ($G=20$), 0.1789 ($G=149$), 0.2563 ($G=215$), 2.6097 ($G=320$), 2.6149 ($G=955$), 3.7124 ($G=3435$) and 3.7213 ($G=4276$), respectively. The maximal fitness greater than or equal to 1.0 means emerging of double negativity.

To systematically characterize S1, we show in Fig. 4 the corresponding dispersion relations, effective constitutive parameters, wave transmission property and pressure magnification. Band structure in Fig. 4(a) displays a single band of $[0.156384, 0.226167]$ with negative curvature. The near-linear trait of the first band indicates the homogenous wave behaviors in the deep-subwavelength scale. The effective parameters in Fig. 4(b) show the simultaneous negative properties for ρ_{eff}^x and K_{eff} within the negative band range illustrated in Fig. 4(a).

The positive values of ρ_{eff}^x and K_{eff} increase simultaneously at the established sampling frequency points (i.e.,

hollow circles and triangles). Indeed, their variations are consistent with the constraints imposed by Eq. (24). More importantly, ρ_{eff}^x and K_{eff} approach their resonance responses near the same frequency of 0.156384, and turn into the negative values simultaneously. This characteristic declares the best opportunity supplied by topology optimization for exploring the broadband double negativity. As plotted in Fig. 4(c), n_{eff}^x and Z_{eff}^x have relatively large values and keep the simultaneous increasing variation as well. Negative n_{eff}^x is generated within the same range as double-negative band in Fig. 4(a). There is a complete bandgap above the negative band, confirming the zero values of $\text{Re}(n_{\text{eff}}^x)$. Using the effective parameters, we can obtain in Fig. 4(a) the retrieved dispersion relations which perfectly match the band structures. The transmission spectrum in Fig. 4(d) shows that regardless of the thickness of the AMM, the total transmission always appears near the lower edge of the double-negative range. In view of the dramatic change in $\text{Re}(Z_{\text{eff}}^x)$ near the lower-edge frequency, the perfectly-matched effective impedance $\text{Re}(Z_{\text{eff}}^x)=1$ should be the physical origin of the total transmission. When the number of unit-cell increases ($N=1, 2, 10$), the Fabry-Perot resonance conditions can be satisfied at more frequencies, consequently causing more standing waves with high transmission compressed within the AMM.

Subsequently, wave transmission based on a microstructure S1 is calculated to demonstrate the essential resonances, see Fig. 4(e). Clearly, the localized pressure generates two peaks with the increase of frequency, confirming the pressure magnification in the region of the upper cavity. To include the influence of the viscous-thermal losses on the material performance, we adopt the simplified equivalent model in Ref. [47] for simplicity. More specifically, we add the loss explicitly into the wavenumber of air as $k_0 = \omega/c_{\text{air}} - \gamma_{\text{loss}} \times i \omega/c_{\text{air}}$

where γ_{loss} is the loss factor. The simulations with the loss factor of 0.004, 0.0093 and 0.022 are performed and depicted in Fig. 4(e). It is obvious that S1 can strike a good balance between the resonance transmission and immunity to dissipation losses.

It is noticed here that we did not adopt the sophisticated thermal-acoustic model considering the viscous-thermal losses for the metamaterials with the Fabry-Perot resonances in Refs. [56-58]. This is based on the fact that the double negativities of the present metamaterials are mainly induced by the overlapping local resonances other than the Fabry-Perot resonances.

Note that the specific resonance mechanisms will be analyzed and discussed in the following section.

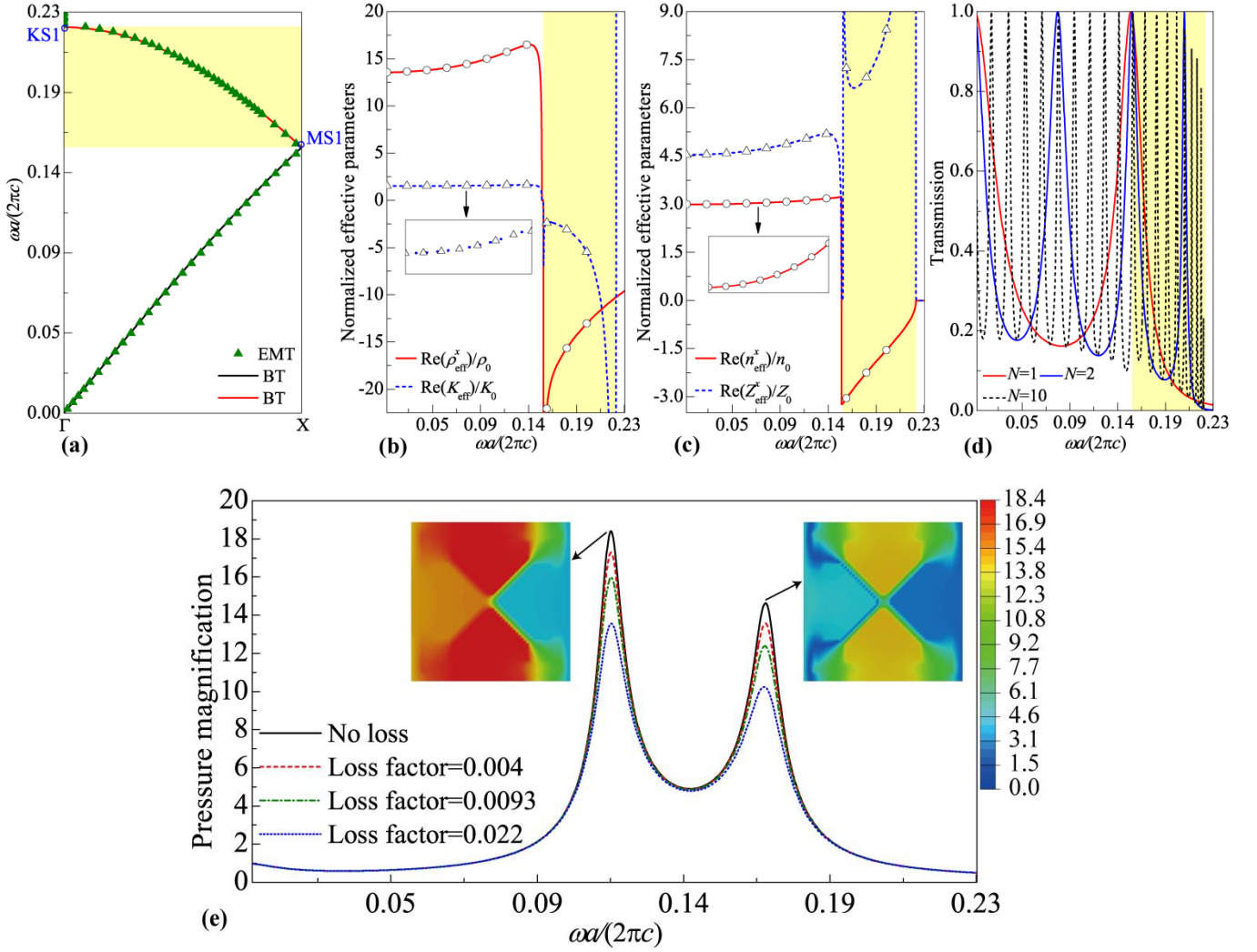


Fig. 4. Various characterizations of topology-optimized AMM S1 in Fig. 2. (a) Band structures along the ΓX direction (solid lines) based on the band theory (BT) and the retrieved dispersion relation $\text{Re}(\mathbf{k})-\omega$ (triangular scatters) based on the effective medium theory (EMT). (b) Relative effective mass density in the x direction and the bulk modulus. (c) Relative effective index and impedance along the x direction. All effective parameters in (b) and (c) are normalized to the background medium. (d) Transmission spectrums of a finite AMM sample with different periodicities N along the x direction for the acoustic plane wave excitation. (e) Frequency dependence of pressure magnification in the region of upper cavity.

3.1.2. Mechanisms of the optimized double negativity

To understand the physics of the double negativity in the resonance-cavity AMMs, we systematically study the eigenstates in the bands of S1-S6, S9 and S13. Figure 5 shows that optimized AMMs support typical LC resonances to guarantee the overlapping of different multipolar (monopolar, dipolar and quadrupolar, etc.) resonances. The eigenstates MS1 and KS1 give the understanding about the physical origin of negative band shown in Fig. 4(a). To be specific, MS2 shows the clear dipolar resonance caused by the highly localized energy in the left and right cavities. The infinite value of the effective mass density in Fig. 4(b) indicates that MS2 is responsible for the negative effective mass density. As for KS2, most energy is localized in four cavities, forming the quadrupolar resonance and causing the infinite effective bulk modulus. Meanwhile, the negative value of K_{eff} in Fig. 4(b) confirms the negative bulk modulus produced by KS2. In this case, the combination of the dipolar and quadrupolar resonances can generate the double negativity. Since the range of negative effective bulk modulus is

smaller than that of the negative effective mass density, the range of the negative effective bulk modulus dominates the bandwidth of double negativity. Similarly, eigenstates MS2 and KS2 also clearly exhibit dipolar and quadrupolar resonances with different locations and occupied spaces of localized energy, respectively. Because the double negativity originates from the overlapping resonances, the double-negative range is determined by the common spaces which can support two kinds of resonances. Consequently, S2 has a smaller double-negative range than S1. Base on the same principle, the resonance space of eigenstate KS3 implies that S3 should have the smallest double-negative range for the square-symmetry case. Unlike the square-symmetry cases, however, MS5 and KS5 show the quadrupolar and hybridization of quadrupolar and monopolar resonances for the negative effective mass density and bulk modulus, respectively. Apparently, their overlapping enlarges the double-negative range. Eigenstate KS6 also shows similar hybridization effect only with different chiral resonance spaces. Nevertheless, MS9 and KS9 indicate that the orthotropic symmetry mainly alters the locations and topologies of the four cavities in the topology optimization, rather than the forms of resonances for double negativity.

To reveal the above LC-resonance mechanisms, we take S1 and S5 in Fig. 2 as examples to illustrate their equivalent physical models ES1 and ES5 in Fig. 5, respectively. In fact, an acoustic resonator is analogous to an inductor-capacitor circuit in terms of resonance properties [2], whose enclosed cavity acts as a capacitor; and relatively narrow air channels as inductor. Obviously, the optimized resonance-cavity-based AMMs can be regarded as a combined system comprising several inductor-capacitor circuits. When pressure variation occurs in the channels, the distributions of the inductors and capacitors determine the excited forms of LC resonances. In other words, the model ES1 can support the eigenstates MS1 and KS1 under two kinds of excitations, yielding the negative mass density and bulk modulus, respectively. However, the model ES5 has different topological feature, i.e., four capacitors locate in the corners and one capacitor in the center. On one hand, this distribution can induce the quadrupolar resonance for negative effective mass density. On the other hand, if five capacitors are excited simultaneously, the hybridization of quadrupolar and monopolar resonance can arise from model ES5 as well.

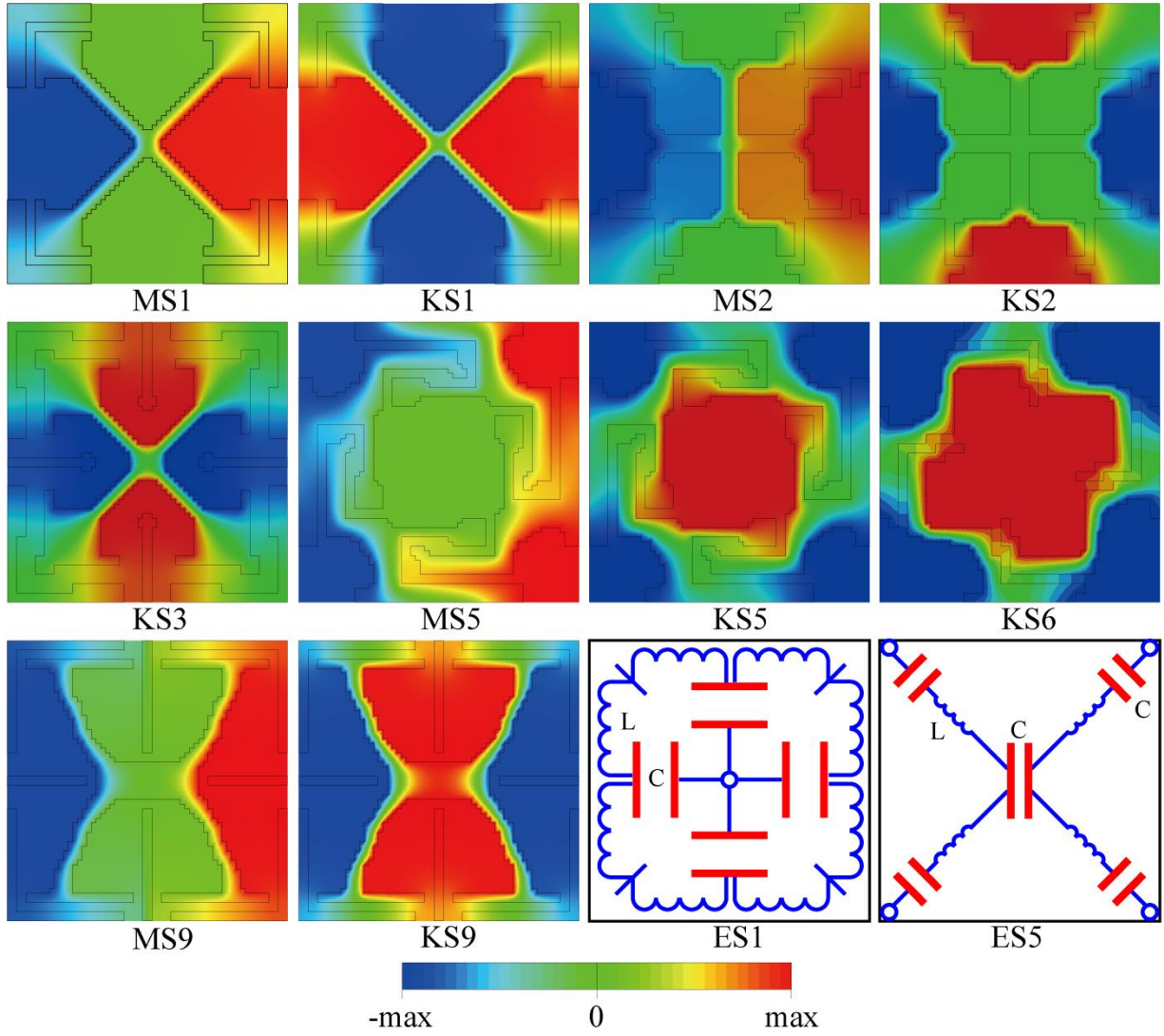


Fig. 5. Specific eigenstates of topology-optimized AMMs S1–S3, S5, S6 and S9. Eigenstates MS1 and KS1 are marked in Fig. 4(a). Eigenstates MS1 (S1), MS2 (S2), MS5 (S5) and MS9 (S9) correspond to the resonant modes, which induce the infinite effective mass density. Eigenstates KS1 (S1), KS2 (S2), KS3 (S3), KS5 (S5), KS6 (S) and KS9 (S9) correspond to the resonant modes, which induce the infinite effective bulk modulus. Sketches ES1 and ES5 represent the equivalent physical models of S1 and S5, respectively.

3.2. Optimized double-negative AMMs under simultaneous non-increasing tendencies of the effective parameters

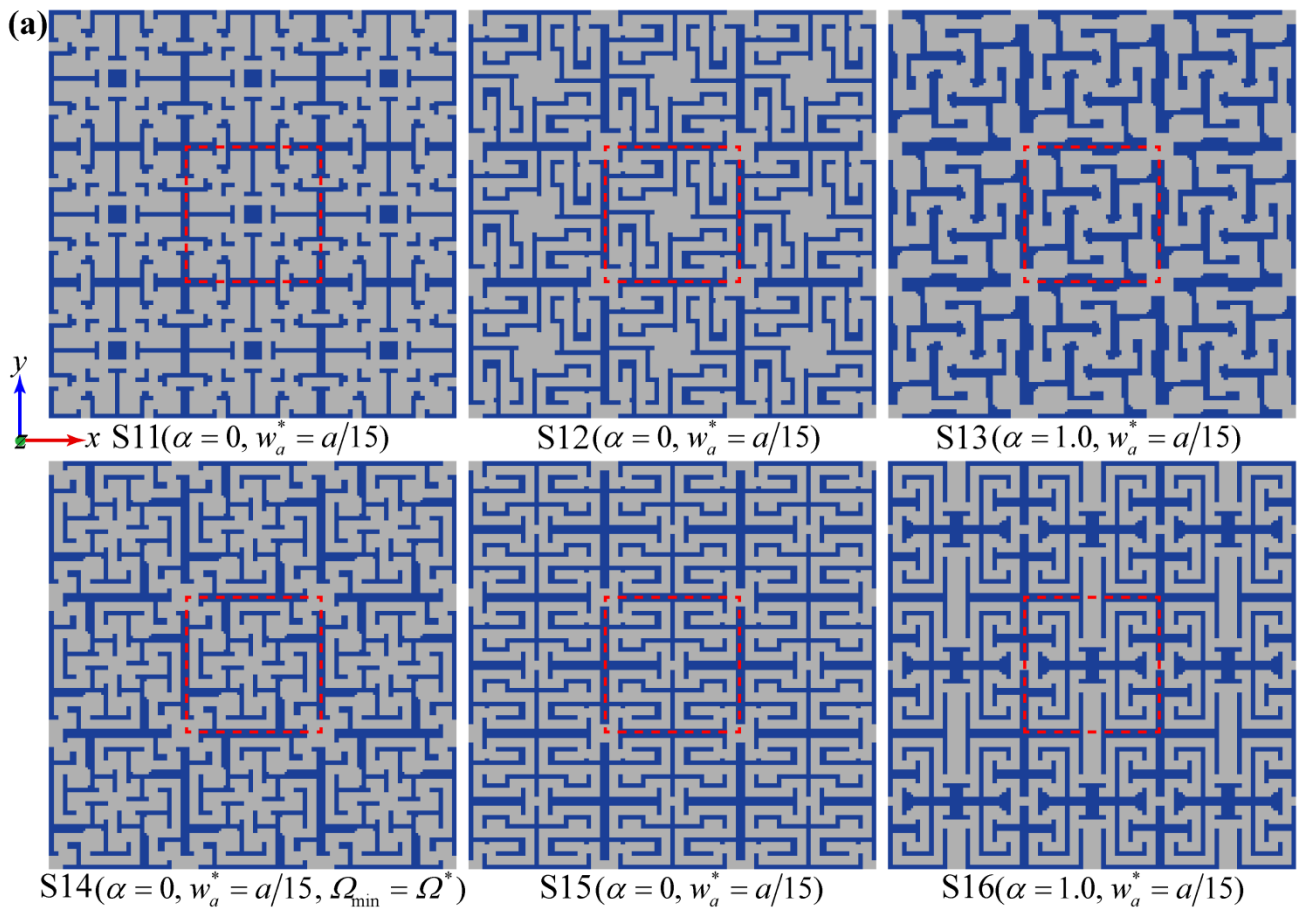
This subsection presents the optimization results with the prescribed simultaneous non-increasing tendencies ($\beta \leq 0$) for both ρ_{eff} and K_{eff} (i.e., case 2 in Eq. (24)). To show the great potential of “non-increasing” mechanism, the optimization uses the more strict geometrical constraint, i.e., w_a^* is set as $a/15$. Similarly, some representative topological features, evolution history, various physical characterizations, negative properties of the optimized metamaterials are analyzed and discussed in details. The emblematic and novel Mie resonances causing the acoustic broadband double negativity are perfectly revealed through the space-coiling AMMs.

3.2.1. Topology-optimized space-coiling AMMs

3.2.1.1 Square, chiral and orthogonal symmetries

Owing to the general feature of the proposed optimization framework in Eqs. (18)-(24), we apply it to design the broadband double-negative AMMs under the simultaneous non-increasing tendencies ($\beta \leq 0$) considering square, chiral and orthotropic symmetries, see Fig. 6. Interestingly, these AMMs exhibit the common topological features essentially different from those shown in Fig. 2: (1) several separated solid blocks in the coiling up space, (2) zigzag air channels forming the labyrinth layouts, and (3) a number of local air regions. Intuitively, like the extreme metamaterials reported by Liang et al. [7], waves can freely propagate inside the curled space with materials of negligible loss, arousing the large phase delays within a small space and then realizing the large refractive index. Consequently, the band folding [7] supporting the double negativity should emerge at the subwavelength scale. Compared with the AMMs in Fig. 2, S11 has more separated solid blocks and complex air channels, achieving the large effective refractive index without the resonance cavities. Note that S11 can only generate the double negativity within [0.25438, 0.379423], see Appendix A. This means that, with the square-symmetry assumption, a better driving force for the low-frequency double negativity should have simultaneous increasing tendencies ($\beta > 0$). However, with the same w_a^* , the chiral- and orthotropic-symmetry AMMs in Fig. 6 offer wider double negativities in the lower frequency ranges. Consequently, the simultaneous non-increasing tendencies ($\beta \leq 0$) are more beneficial for the low-frequency broadband double negativity than the increasing tendencies ($\beta > 0$). In addition, both the optimized chiral- and orthotropic-symmetry AMMs can deliver the preferable double negativity. This testifies the robustness of the space-coiling topology for generating double negativity. The comparison of S12 and S13 shows that increasing α can reduce the air paths and induce the thinner hard solid plates. Since S14 is generated with the different target spectra, similar topology and double negativity of S14 demonstrate that the proposed optimization strategy is robust for specific frequencies. Results in Fig. 6(b) also show that wide air regions, except the interconnection core regions, and relatively thick hard solid plates can result in the degenerations of double negativity. Therefore, the most beneficial space-coiling topology should include suitable zigzag channels, thin curved hard solid plates and interconnection core regions in the center.

To further check the negative properties of the space-coiling AMMs in Fig. 6(a), Figure 6(b) presents their double-negative ranges and quasi-static refractive index and impedance. For the low-frequency performance, the optimized AMMs, S12, S14, S15 and S16, have the conspicuous broadband double negativity transcending the previous extreme metamaterials [7]. Moreover, all optimized space-coiling AMMs in Fig. 6 possess larger air channels than those of the previous extreme metamaterials [7, 46], thus obviously reducing the viscous loss. In spite of the more strict constraints on air channels than those in Fig. 2, the optimized AMMs in Fig. 6 can also provide the desired negative bands. With the same symmetry, the variations of the impedance are positively related to refractive index. Differences between S12, S14, S15 and S16 show that the orthotropic-symmetry AMMs can generate similar refractive index with the chiral-symmetry ones. However, the corresponding impedance will be obviously increased. This further illustrates that the chiral symmetry can result in ideal double negativity and wave transmission simultaneously. For the chiral symmetry, the difference between the performance of S12 and S13 shows that a relatively large α can induce a smaller refractive index and impedance, causing a relatively small double-negative range. In the other words, the variation of the refractive index dominates the optimization in this case. However, for the orthotropic symmetry, the relatively large α mainly reduces the dispersion extent of ρ_{eff}^x and K_{eff} , resulting in a smaller double-negative range.



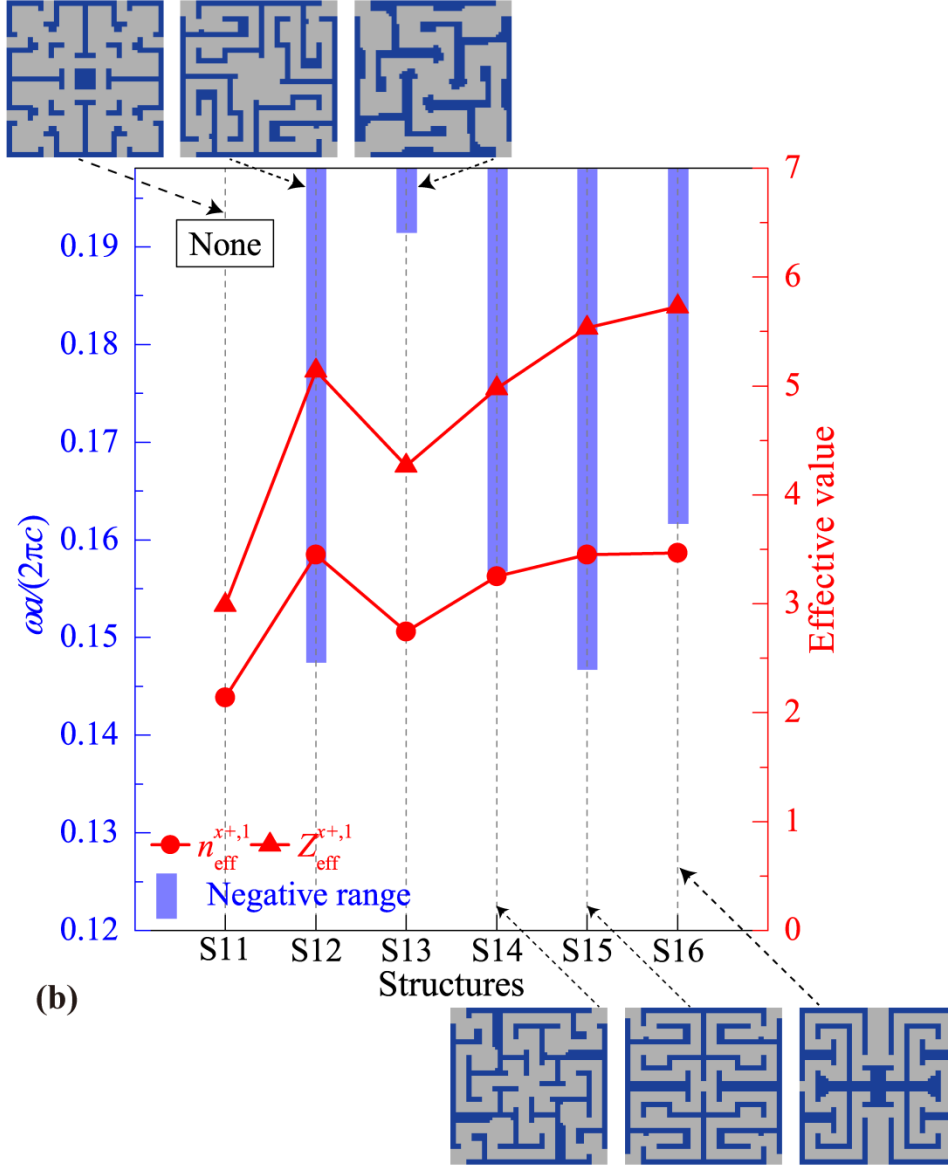


Fig. 6. Topology-optimized space-coiling AMMs with three representative symmetries. (a) Optimized microstructures. All topology-optimized metamaterials are under the constraint of $\beta \leq 0$. The target spectrum of S14 is selected as $[0.09903, 0.198061]$ (i.e., $\Omega^* = 0.09903$). The ranges of the other structures are set as $[0.002476, 0.198061]$. For the microstructures S15 and S16, to guarantee the isotropy of effective bulk modulus, the relative difference between K_{eff} retrieved from the x direction and y direction wave simulations are forced to be smaller than 5%. (b) Comparisons of double negativities, the quasi-static effective refractive index n_{eff}^{x+1} and impedance Z_{eff}^{x+1} at Ω_{min} for S11-S16. More performances are summarized in Appendix A.

With the prescribed typical symmetries, the present topology optimization can effectively realize the novel space-coiling microstructures having ideal double negativity, which breaks the restrictions of single negativity [47] or narrow-band double negativity of the labyrinth metamaterials [7]. From the prospective of double negativity, both the chiral and orthogonal symmetries provide an attractive and effective design approach, outperforming the square symmetry. From the prospective of topological features, three symmetric AMMs share the common ground for negative properties: suitable zigzag channels, thin curved hard solid plates and interconnection core regions in

the center. Mindful of the manufacturing difficulty, it is easy to fabricate all space-coiling microstructures containing mainly straight hard solid plates.

3.2.1.2 Analysis of representative AMM S12

To understand the origin of the space-coiling topology shown in Fig. 6, we show the evolutionary history of the maximal fitness with the generation number for the AMM S12 in Fig. 7. The noteworthy change from the generation $G=0$ ($F=0$) to $G=10$ ($F=0.2859$) illustrates the strong searching ability of the GA in determining the separated thick hard solid plates and interconnection core regions. The creation of the double negativity at generation $G=117$ ($F=1.5521$) suggests that making channels and solids parts more curved is an effective way for getting double negativity. From $G=117$ ($F=1.5521$) to $G=4680$ ($F=4.0818$), the solid components become thinner while the curved portion of the zigzag paths increases, thus producing a bigger double negativity range. Meanwhile, the interconnection core region in the center maintains a relatively large size. In spite of the similar space-coiling topology with the extreme metamaterials reported by Liang et al. [7], the AMM S12 shows the emblematic features of larger interconnection regions and more curved degree of the hard solid plates, which gives rise to better double-negative property.

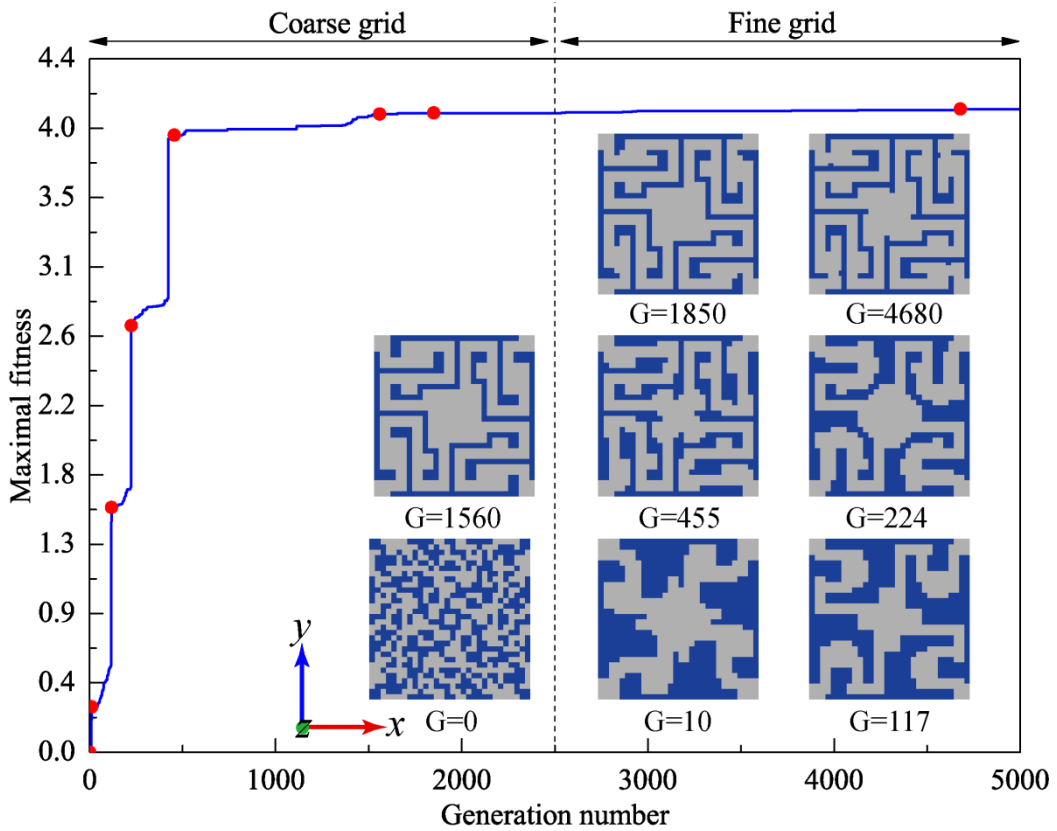


Fig. 7. Evolutionary history for the generation of topology-optimized AMM S12 in Fig. 6. Illustrations display eight representative topologies during the “coarse to fine” optimization. The objective function values of eight microstructures are 0 ($G=0$), 0.2859 ($G=10$), 1.5521 ($G=117$), 2.7063 ($G=224$), 3.9155 ($G=455$), 4.0487 ($G=1560$), 4.056 ($G=1850$) and 4.0818 ($G=4680$), respectively.

To characterize the double negativity of S12, we systematically study the dispersion relations, effective parameters and transmission spectrum, see Fig. 8. For the second band range displayed in Fig. 8(a), the different physical quantities coincide mutually. Interestingly, owing to the band folding, the slopes around the Γ point in both the ΓX and ΓM directions are almost the same in the first, second, fourth, sixth, eighth and tenth bands. In fact,

this band folding not only indicates the isotropic indices, but also gives rise to the ideal negative properties at both subwavelength and long-wavelength regimes. Just as the constraints of simultaneous non-increasing tendencies in Eq. (24), the positive ρ_{eff}^x and K_{eff} decrease simultaneously below the negative range. The simultaneous negative ρ_{eff}^x and K_{eff} in Fig. 8(b) and negative n_{eff}^x clearly demonstrate the double-negative property of the negative band depicted in Fig. 8(a). Unlike the results in Fig. 8(b), the positive n_{eff}^x and Z_{eff}^x have the opposite variation patterns. Using the effective parameters in Figs. 8(b) and 8(c), the retrieved dispersion relations based on EMT can perfectly match the band structures. Benefitting from the perfectly-matched effective impedance $\text{Re}(Z_{\text{eff}}^x)=1$, total transmission appears near the lower edge of the double-negative range no matter whether the metamaterial layer is thin ($N=1, 2$) or thick ($N=10$), see Fig. 8(d). Besides, the high transmission at other frequencies can also be obtained because of the satisfied Fabry-Perot resonance conditions.

The wave transmission based on a microstructure of S12 is further calculated to demonstrate the essential resonances, as shown in Fig. 8(e). Clearly, large magnitude pressure is mainly localized in the central interconnection region, showing a pressure magnification in the region of the upper cavity. Obviously, S12 allows striking a good balance between the resonance transmission and immunity to dissipation losses. Note that the specific resonance mechanisms will be analyzed and discussed in the following section.

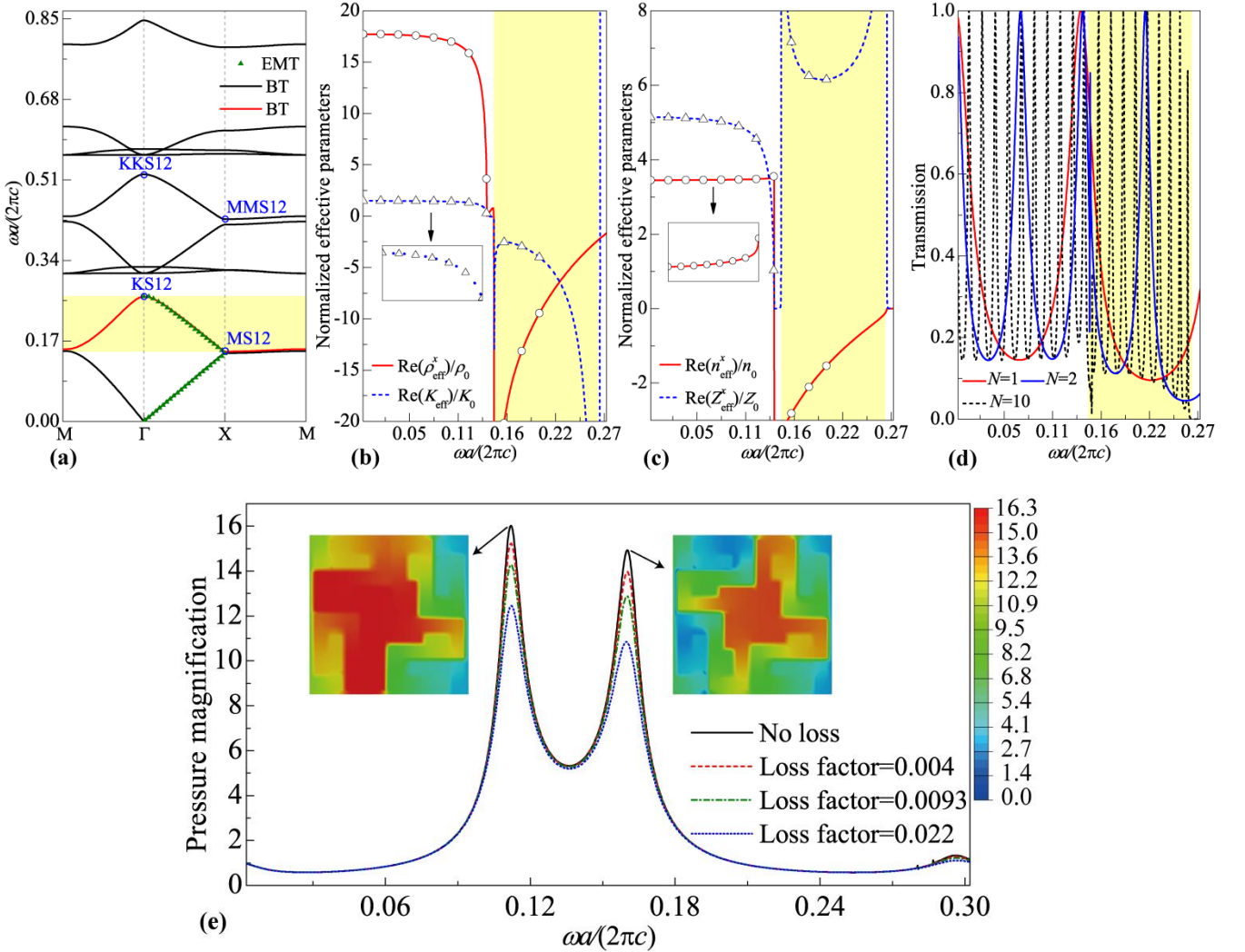


Fig. 8. Various characterizations of AMM S12 in Fig. 6. (a) Band structures (solid lines) based on the band theory (BT) and the retrieved dispersion relation $\text{Re}(\mathbf{k})-\omega$ (triangular scatters) based on the EMT. **(b)** Relative effective mass density in the x direction and the bulk modulus. **(c)** Relative effective index and impedance along the x direction. All effective parameters in (b) and (c) are normalized to the background medium. **(d)** Transmission spectrums of a finite AMM sample with different periodicities N along the x direction for the acoustic plane wave excitation. **(e)** Frequency dependence of pressure magnification in the region of central interconnection core.

3.2.2. Mechanisms of optimized double negativity

To reveal the origin of the double negativity in the space-coiling AMMs, we take four metamaterials S12-S15 as examples and scrutinize their specific eigenstates in Fig. 9. Obviously, eigenstates MS12 and KS12 portray the quadrupolar and hybridization of quadrupolar and monopolar Mie resonances which can essentially induce the negative effective mass density and bulk modulus, respectively. It is relevant to note that these artificial Mie resonances distinctly differ from the LC resonances shown in Fig. 5. In principle, the Mie resonance usually appears in the structure having a high refractive index relative to the background medium [27, 47]. Instead of highly localizing all energy within several cavities, the Mie resonances enable energy concentration in the air regions while producing apparent radiation, showing the feature of resonance scattering. Eigenstates MMS12 and KKS12 behave like a second-order quadrupolar and hybridization of the quadrupolar and monopolar Mie resonances, and characterize the double-negative essence of the sixth band in Fig. 8(a). Similarly, the high-frequency negative band (tenth band) in Fig. 8(a) also has the double negativity resulted from the higher-order Mie resonances. Eigenstates MS13 and KS13 also show that the double negativity of S13 is generated by the quadrupolar and hybridization of the quadrupolar and monopolar Mie resonances. Comparing the field distributions of MS12, KS12, MS13 and KS13, we can infer that the relatively large interconnection core region will cause the double negativity in the lower frequency range, see the negative ranges of S12 and S13 shown in Fig. 6(b). In addition, eigenstates MS14 and KS14 show that the Mie resonances can also be induced by more complex labyrinth structures. This means that the space-coiling topology is very robust for generating the multipolar Mie resonances. In addition, eigenstates MS15 and KS15 show that the ortho-symmetric labyrinth topology is conducive to similar Mie resonances as well. Hence the AMMs presented in Fig. 6 provide unanticipated topological features for both Mie resonances and double negativity. Note that the bandwidth of the double negativity is determined by the size of the overlapping regions for two resonances. However, in case of the quadrupolar and hybridization of the quadrupolar and monopolar Mie resonances, the largest overlapping regions should be the four corner areas, which indicates the corresponding limited bandwidth. In particular, it is the combination of multipolar resonances that provide the broadband double negativity over the previous studies on space-coiling AMMs [7]. Overall, eigenstates in Fig. 9 disclose that the optimal mechanism with space-coiling topology for broadband low-frequency double negativity should be the combination of quadrupolar and hybridization of quadrupolar and monopolar Mie resonances.

To reveal the above Mie-resonance mechanisms, we also present in Fig. 9 the equivalent physical models ES12 and ES13 of the AMMs S12 and S13, respectively. Because S12 has the high effective refractive index and an air cavity in the center, the whole microstructure can be equivalent to four channels composed of the ultraslow medium connected with an air interconnection core. And they are separated by the solid frame materials. When waves propagate in the four channels with different phases, the model ES12 can produce the quadrupolar Mie resonance MS12 or the hybridization of the quadrupolar and monopolar Mie resonance KS12. In particular, the relatively large interconnection core further promotes this hybridization. Since the holistic effective refractive index of S13 is smaller than that of S12, the corresponding equivalent model ES13 has different straightened channels while ensuring similar geometrical feature. In addition, since S13 has smaller air cavities in the center than S12, ES13 should have smaller air interconnection core as well. As a result, the difference between ES12 and

ES13 mainly affects the frequency range of double negativity.

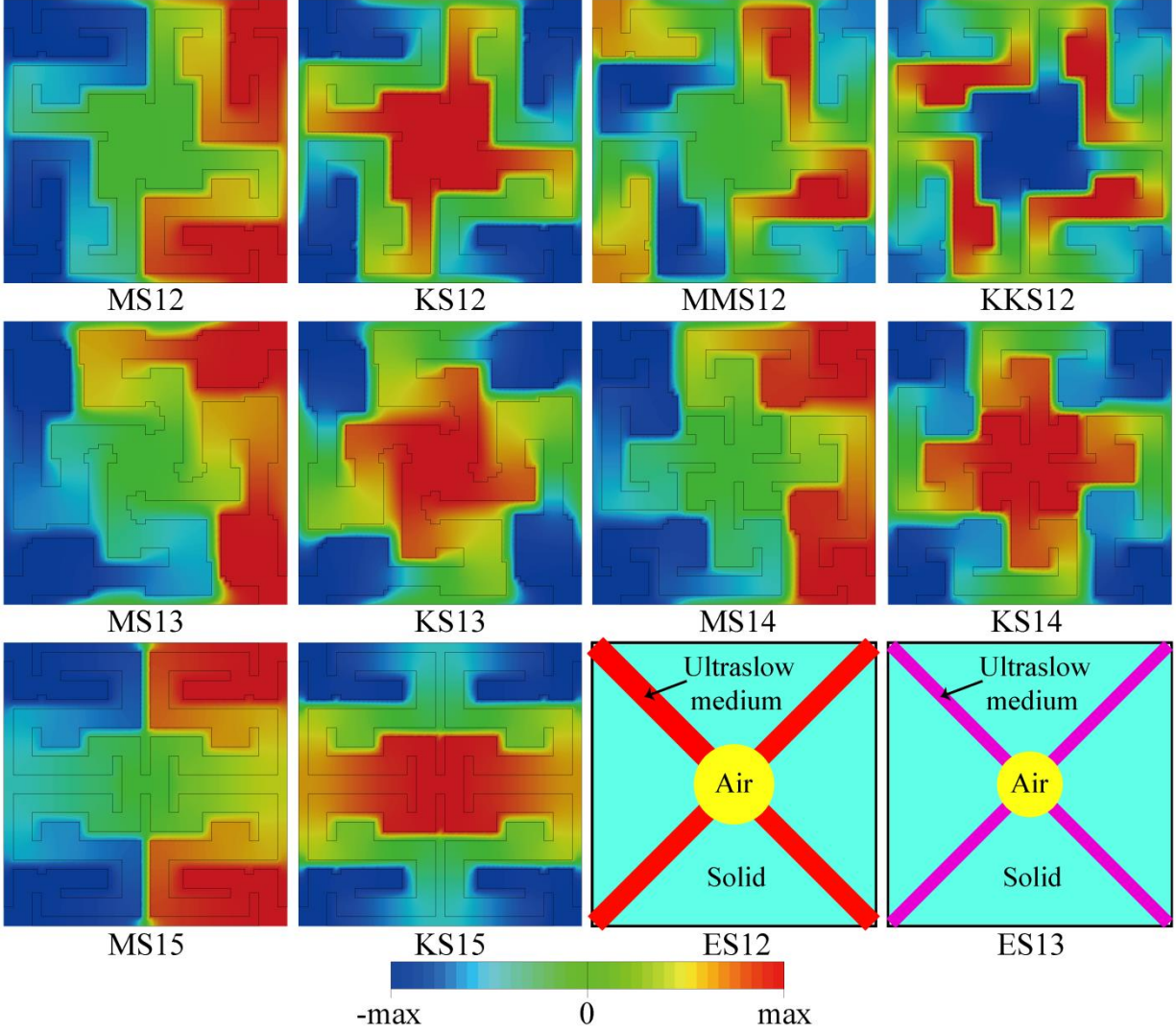


Fig. 9. Specific eigenstates of topology-optimized AMMs S12-S15. Eigenstates MS12 and KS12 are marked in Fig. 8(a). Eigenstates MS12 (S12), MMS12 (S12), MS13 (S13), MS14 (S14) and MS15 (S15) correspond to the resonant modes, which induce the infinite effective mass density. Eigenstates KS12 (S12), KKS12 (S12), KS13 (S13), KS14 (S14) and KS15 (S15) correspond to the resonant modes, which induce the infinite effective bulk modulus. Sketches ES12 and ES13 represent the equivalent physical models of S12 and S13, respectively.

3.3. Brief summary on two categories of AMMs

Due to the tremendous inverse-design ability, topology optimization has explored two categories of novel AMMs with broadband double negativity, namely the resonance-cavity-based and space-coiling metamaterials, respectively. For the desired negative properties, the space-coiling metamaterials can realize a wider double negativity within the lower frequency ranges, showing superiority over the resonance-cavity-based ones. In addition, the double negativity of the space-coiling metamaterials is less affected by the width of the air channels. And space-coiling metamaterials can produce the double negativity by introducing larger air channels. A good resonance-cavity-based metamaterial should possess the multiple air resonance cavities, several hard solid plates and air channels. For the space-coiling metamaterials, the beneficial topologies should include the suitable zigzag channels, thin curved hard solid plates and interconnection core regions in the center. For the double-negative

mechanisms, the resonance-cavity-based metamaterials benefit from the novel multipolar LC resonances. But the space-coiling metamaterials support the novel multipolar Mie resonances. In principle, both novel mechanisms overcome the limitations of the reported negative resonances [2, 7, 25, 46-47], representing the optimal physical essences for broadband double negativity so far. Because of the most straight hard solid plates, the space-coiling metamaterials are easier to be manufactured than the resonance-cavity-based ones. Anyway, the topology-optimized AMMs presented in this paper can achieve the double negativity in a brand-new structural style.

3.4. Potential applications using topology-optimized double-negative AMMs

This subsection presents the numerical results of broadband double negativity and the enhancement of evanescent wave transmission for LC-resonance and Mie-resonance optimized AMMs. Then we respectively show the negative refraction and acoustic subwavelength imaging with high transmission. Finally, the experimental demonstration of subwavelength imaging is successfully realized.

3.4.1. Numerical demonstrations of wave behaviors

To demonstrate the desired negative dispersions, we illustrate the equi-frequency surfaces (EFSs) of metamaterials S1 and S12 in Figs. 10(a) and 10(b), respectively. It is noted that two negative bands show the quite isotropic behavior within the whole range except the lower edge of the bands with the slight anisotropy. In addition, we can clearly observe the striking difference between the LC-resonance and Mie-resonance negative bands in Figs. 4(a) and 8(a), i.e., two bands are arc-shaped and nearly-straight, respectively. The variations of the EFSs with the increasing frequency in Figs. 10(a) and 10(b) suggest that the negative group velocities should occur along all directions. When waves are incident to the interface between the AMMs and background media, the refracted group velocity should be pointed to the direction of frequency increasing which is perpendicular to the contours, causing the expected negative direction. It is worth mentioning that the target frequency spectrum of [0.002476, 0.198061] can guarantee the all-angle negative refraction for the whole target frequency spectrum. Then the subwavelength imaging can be realized within the whole target frequency spectrum as well.

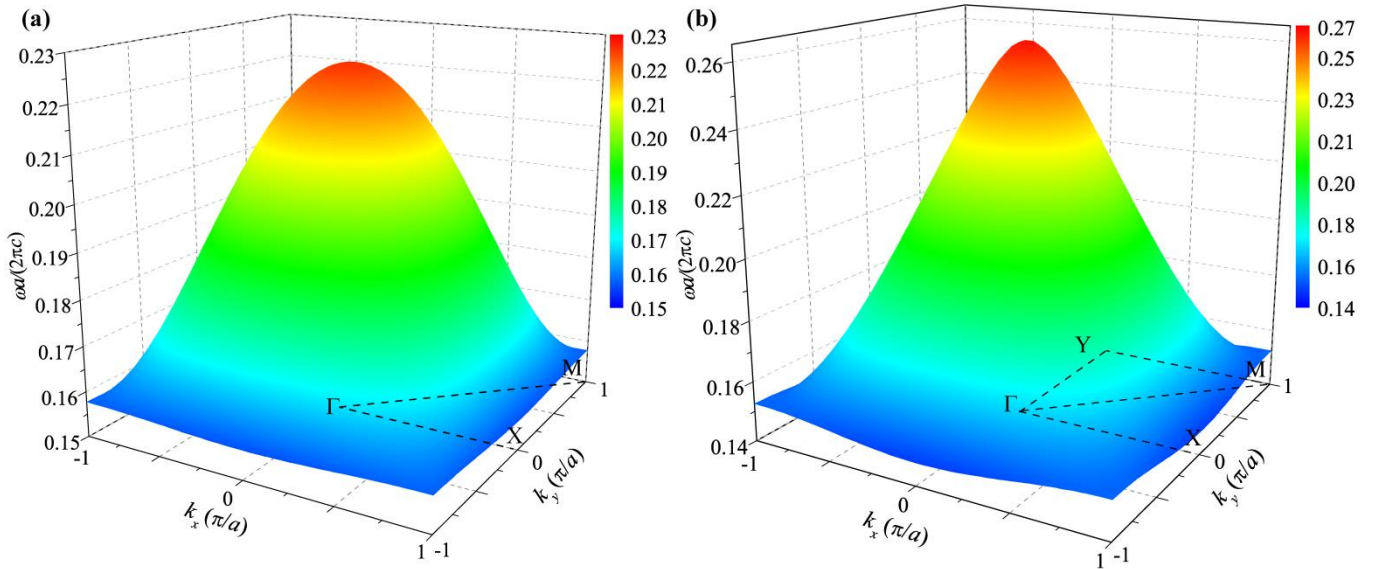


Fig. 10. Equi-frequency surfaces of topology-optimized AMMs. Surface plots of the first negative band (the second band) over the whole Brillouin zone for S1 (a) and S12 (b).

To validate the negative refraction and subwavelength imaging, we display the corresponding simulation results for the metamaterials S1 and S12 in Figure 11. As predicted in Figs. 11(a) and 11(c), when the Gaussian beam (45°) of an acoustic wave is incident from the left region, the desired negative refraction with high transmission can be clearly observed at $\Omega=0.173303$ and $\Omega=0.160925$, respectively. Since a recent study found that the acoustic-structural interaction may have a certain effect in the space-coiling AMMs [58], we display the numerical simulations with considering the acoustic-structural interaction in Figs. 11(b) and 11(d). The nearly identical beam patterns demonstrate that the acoustic-structural interaction has only a very slight effect on the wave propagation properties of the optimized AMMs in this study. Meanwhile, when a point source is excited in the left of the metamaterial slab, obvious imaging effect for S1 and S12 can be observed in the exiting surfaces of the slabs in Figs. 11(e) and 11(f). Their full widths at the half maximum (FWHM) of images are 0.44λ and 0.39λ , respectively, which are beyond the diffraction limit. Therefore, topology-optimized metamaterials S1 and S12 are demonstrated to have the ability of realizing the subwavelength imaging. In addition, we also present the simulations for S12 at the different frequencies in Figs. 11(f)-11(i). Comparisons between the results in Figs. 11(f)-11(i) show that the metamaterial lens can effectively generate the stable subwavelength imaging within the negative range. With the increase of frequency, the imaging resolution decreases and more energy is reflected by the lens due to the inevitable impedance mismatch.

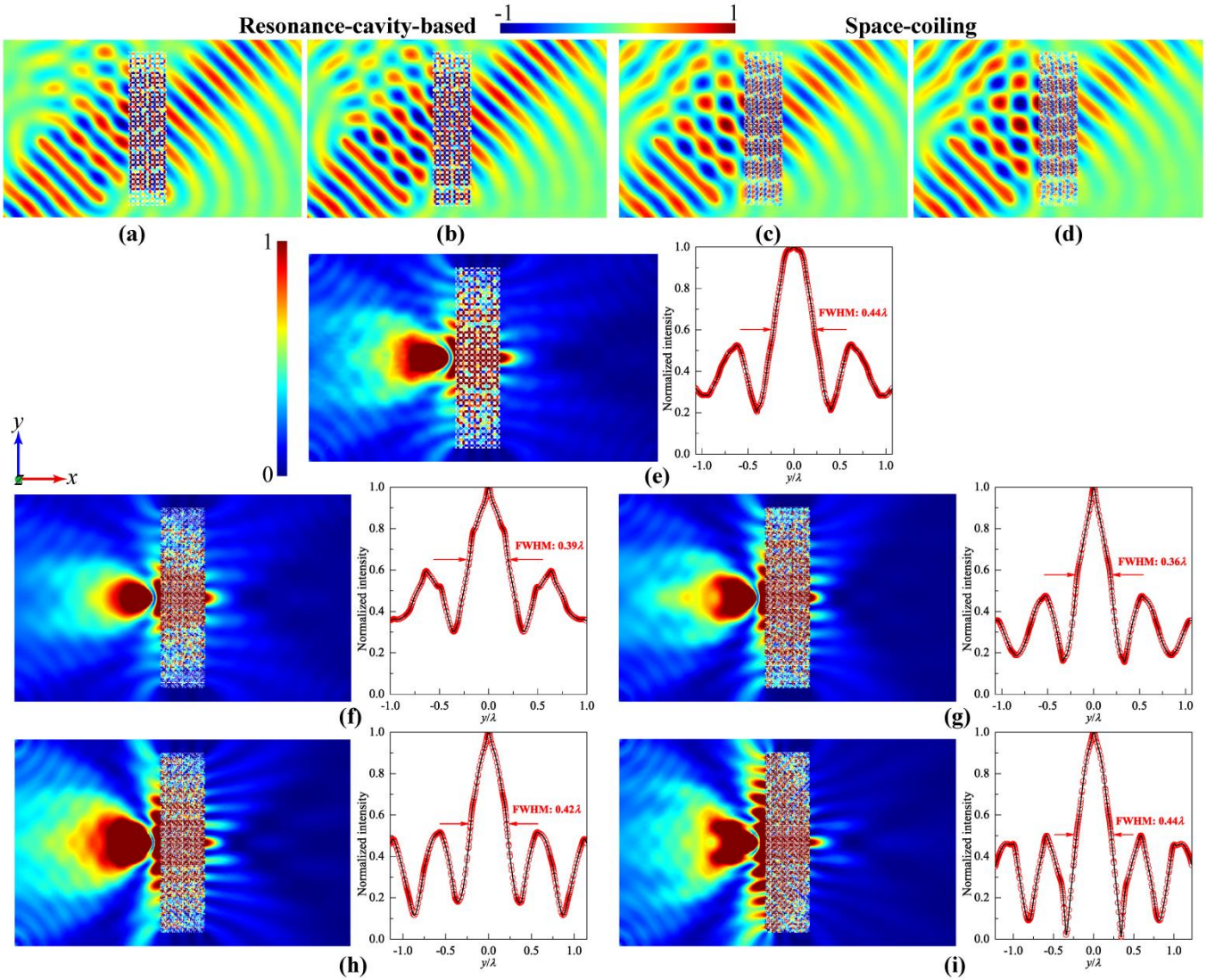


Fig. 11. Simulations of negative refraction and acoustic subwavelength imaging using topology-optimized AMMs. (a)-(d) Pressure fields under an incident Gaussian beam (45°) of acoustic waves for S1 without (a) or with (b) considering the acoustic-structural interaction

at $\Omega=0.173303$ and S12 without (c) or with (d) considering the acoustic-structural interaction at $\Omega=0.160925$, respectively. (e) Imaging field pattern and intensity profiles (the source is located at the position a away from the left side of the 32×8 metamaterial slab) for S1 at $\Omega=0.173303$ (FWHM=0.44 λ). (f)-(i) Imaging field patterns and intensity profiles for S12 at $\Omega=0.160925$ (FWHM=0.39 λ) (f), 0.173303 (FWHM=0.36 λ) (g), 0.185682 (FWHM=0.42 λ) (h) and 0.198061 (FWHM=0.44 λ) (i), respectively.

To establish the subdiffraction-limit resolution in Fig. 11, we present in Fig. 12 the zero-order transmission coefficient [2, 23-24] of a plane wave for evaluating the transmission of both propagating and evanescent waves through an 8-layered metamaterials of S1 or S12 immersed in air. Note that a value of zero-order transmission larger than 1.0 implies the enhancement of the propagating or evanescent waves. The regions representing the propagating waves locate in the left of the skew lines in Figs. 12(a) and 12(b). And the regions located in the right of the skew lines describe the case of evanescent waves. For every frequency within the double-negative range, it is clear that the transmission coefficient can be larger than 1.0 for the wave vector k_y , either near or far away from k_0 . And the lower-frequency range has the enhancements in the wider range of k_y than the higher-frequency one. This emphasizes the importance of the frequency in enhancing evanescent waves for imaging. Consequently, benefiting from the enhancement of evanescent waves, the metamaterial lens can capture the subwavelength information of the object and then transfer the corresponding energy to the focal plane of the image.

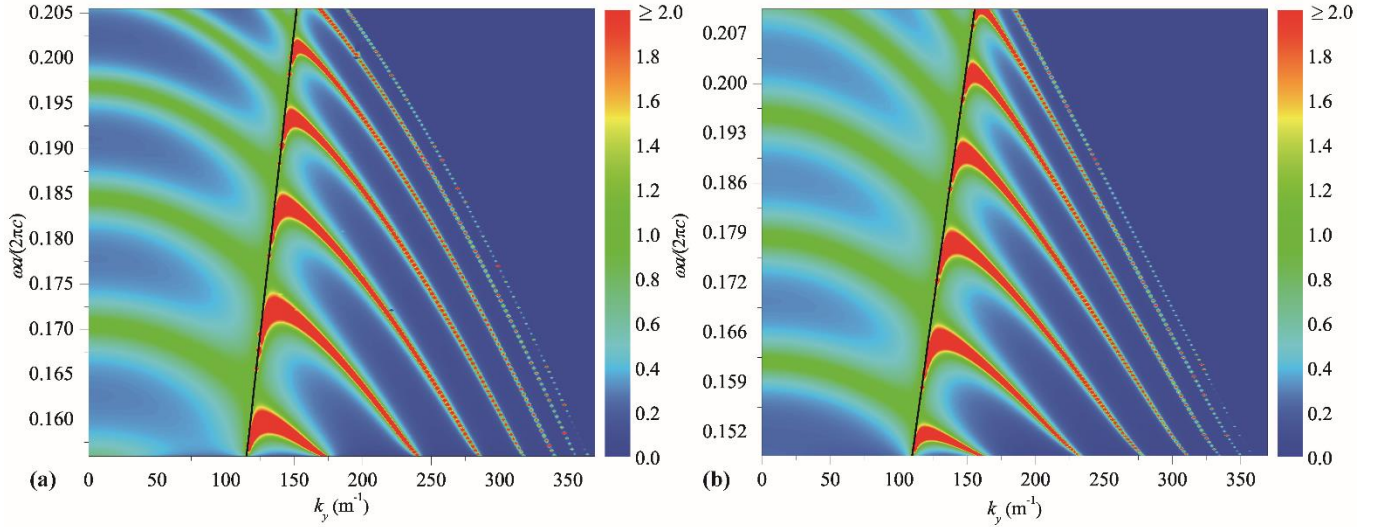


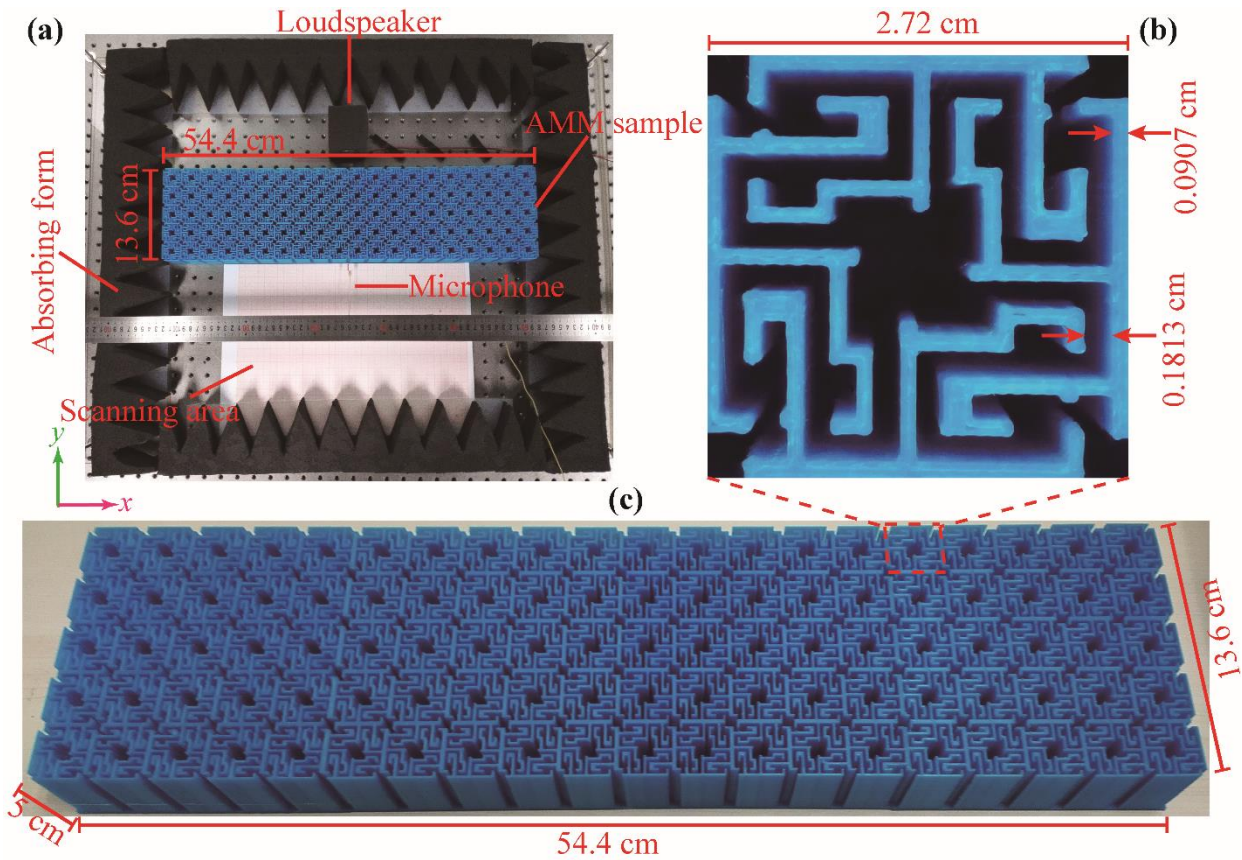
Fig. 12. Enhanced transmission of the evanescent waves through topology-optimized AMMs. Frequency and wave-vector dependence of the zero-order transmission coefficient for both propagating and evanescent waves through a layer consisting of 8 metamaterials S1 (a) or S12 (b). Two skew lines in (a) and (b) represent the dispersion curves for air. If $k_y \leq k_0$ (k_0 is the propagation constant of the fundamental waveguide mode), the transmission coefficient characterizes the transmission property for the propagating waves, while for $k_y > k_0$ the corresponding waves represent the evanescent waves.

3.4.2. Experimental verification of acoustic subwavelength imaging

Above results show that the space-coiling AMMs can realize the ideal broadband double negativity with relatively large air channels. In addition, they are mainly composed of straight hard solid plates, showing good workability. To show the convincing potential of the optimized AMMs, we worked with the space-coiling AMM S12 and experimentally demonstrated the broadband subwavelength imaging in Fig. 13. We adopted 3D-printing to fabricate an AMM sample made of polylactide acid (PLA) with a mass density of 1250 kg/m^3 and bulk modulus $3.5 \times 10^9 \text{ Pa}$. The fabricated metamaterial slab in Figs. 13(a) and 13(c) consists of 20×5 microstructures depicted in Fig. 13(b). Experimental apparatus for the acoustic experiment inside a waveguide is illustrated in Fig. 13(a) where the slab sample was surrounded by the acoustic absorbing foams to avoid reflections. A loudspeaker,

located 3cm away from the input interface of the slab, was used as the point source of waves; while the mounted microphone measured the acoustic pressure by moving in the scanning area. Signals at each position were averaged over four measurements. Using the Fourier transform, the whole acoustic field was obtained after the scanning measurement.

We first tested the subwavelength imaging of the metamaterial slab at 2200 Hz which is within the double-negative frequency range. The measured results in Fig. 13(e) agree well with the simulation results in Fig. 13(d) in terms of the acoustic magnitude for the dashed area. The measured results at 2350 Hz in Fig. 13(f) also show the desired imaging pattern. The measured imaging resolutions of Figs. 13(e) and 13(f) are 0.38λ and 0.44λ , respectively, certifying the subwavelength property well. Then we study the performance of the subwavelength imaging within the range of [1700Hz, 2500Hz], as displayed in Fig. 13(g). One peak with high transmission can be clearly observed at all measured frequencies, demonstrating the broadband characteristic of the subwavelength imaging. Moreover, the non-monotonic curve in Fig. 13(h) exhibits all imaging resolutions less than or equal to the diffraction limit. Overall, the low operating frequency is beneficial to the high resolution. Clearly, the measured subwavelength imaging in Fig. 13 is attributed to the double negativity of the metamaterials.



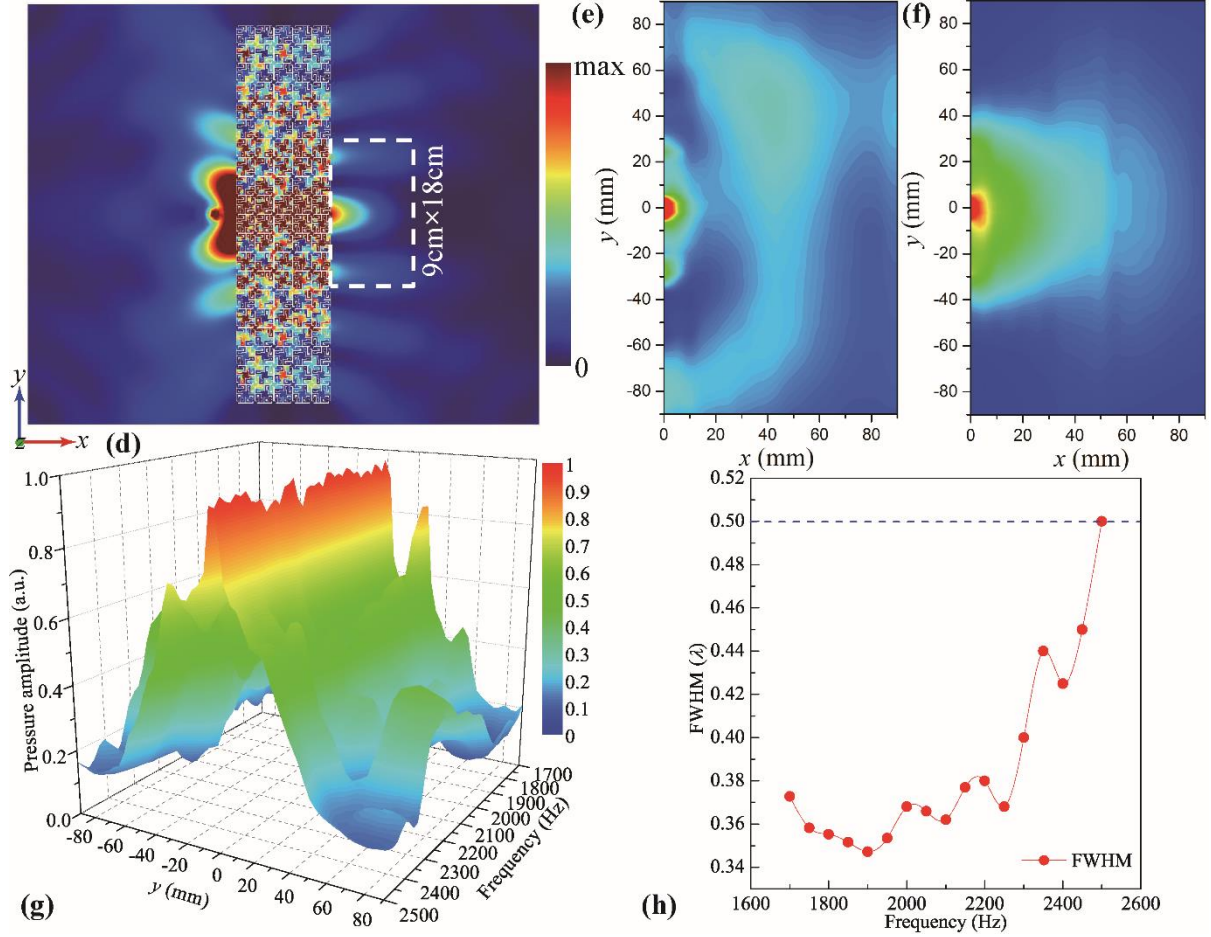


Fig. 13. Experimental demonstration of acoustic subwavelength imaging using topology-optimized AMM S12. (a) Experimental apparatus. A loudspeaker acting as a point source is placed 3cm away from the metamaterial slab. (b) Fabricated 3D-printing microstructure of S12 using the polylactice acid (PLA). (c) Top view of the metamaterial slab. (d) Simulation result of 20×5 metamaterial slab based on S12 at 2200 Hz. (e)-(f) Measured magnitude fields at 2200 Hz (e) and 2350 Hz (f) of the dashed region in (d). Their corresponding imaging resolutions are $\text{FWHM} = 0.38\lambda$ (e) and $\text{FWHM} = 0.44\lambda$ (f), respectively. (g) Measured magnitude fields along the exiting surface of the metamaterial slab within the operating frequency range of [17000 Hz, 2500 Hz]. (h) Measured imaging resolutions within the operating frequency range.

4. Conclusions

In summary, for the first time, we construct a unified topology optimization framework for systematic designing the double negativity with any manual requirement including the expected microstructure symmetry, derivable double-negative mechanisms, necessary structural feature sizes and dispersion extent control of effective parameters. We design various novel microstructures with broadband double negativity and reveal the most beneficial topological features of resonance-cavity-based and space-coiling metamaterials. One feasible design principle is the suitable assembling of multiple air resonant cavities, solid blocks and air channels for resonance-cavity-based structures. Alternatively, one can realize suitable combinations of zigzag channels, thin curved hard solid plates and interconnection core regions in the center. Exhaustive characterizations of the metamaterials indicate that the double negativity, originating from the novel multipolar LC or Mie resonances, can be induced by the simultaneous increasing or non-increasing mechanisms in optimization. Desired acoustic negative refraction and subwavelength imaging of the optimized AMMs are numerically demonstrated in details for two representative AMMs. The enhancements of evanescent waves propagating through the metamaterials are

found to be responsible for the subdiffraction-limit imaging resolution. In addition, we also experimentally validate the broadband subwavelength imaging of the space-coiling AMMs.

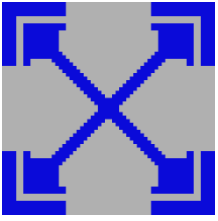

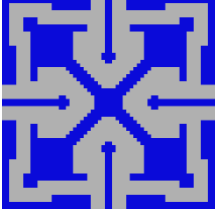
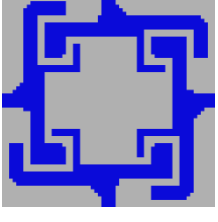

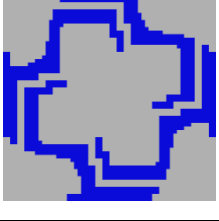
More importantly, the proposed topology optimization framework, involving the derivable LC and Mie resonances, is not restricted to the double negative metamaterials presented here. In principle, the design strategy proposed here can be universal and applicable to other types of AMMs demanding negative constitutive parameters, no matter whether they are double-negative [26-30], single-negative [2, 23, 40] or even hyperbolic [23-24, 35]. The present optimized AMMs and superlens provide the subwavelength imaging with powerful and heuristic components, pushing the conceptual design to the specific practical applications. Our future work will focus on the in-depth design and realization of three-dimensional double-negative AMMs by topology optimization.





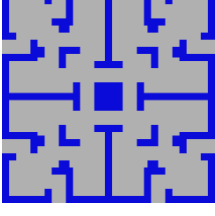
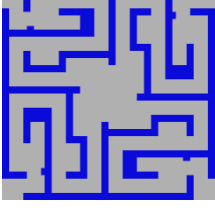
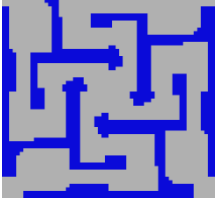
Finally, we would like to mention that the present optimization excludes the effect of the viscous-thermal losses. Although our experimental results show that the double negativities are not visibly affected by the viscous-thermal losses, at least for the samples used in our experiments, the effect of the viscous-thermal losses on topology optimization is an interesting topic for the future work.

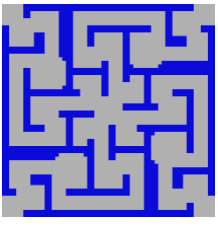
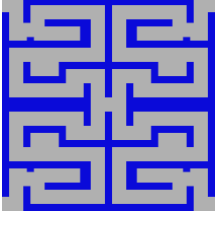
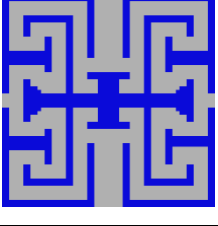
Acknowledgements

This work is supported by the National Natural Science Foundation of China (Grant Nos. 11802012 and 11532001), Project funded by China Postdoctoral Science Foundation (2017M620607) and the Sino-German Joint Research Program (Grant No. 1355) and the German Research Foundation (DFG, Project No. ZH 15/27-1). H. W. Dong is also supported by the Fundamental Research Funds for the Central Universities (FRF-TP-17-070A1). H. W. Dong would like to thank Dr. Chen Shen (Duke University, USA) and Prof. Rui Zhu (Beijing Institute of Technology, P. R. China) for their helpful discussions.

Appendix A. Performances of the optimized AMMs with double nativities

Number of structures	Topology of microstructures	Mechanism (Resonance)	Double-negative range in the target spectrum	Negative range beyond the target spectrum	Key optimization parameter
S1		LC $\rho < 0$: Dipolar $K < 0$: Quadrupolar	[0.156384, 0.198061]	[0.198061, 0.226167]	$\alpha = 1.0$ $w_a^* = a/30$ $\beta > 0$
S2		LC $\rho < 0$: Dipolar $K < 0$: Quadrupolar	[0.177318, 0.198061]	[0.198061, 0.312607]	$\alpha = 1.5$ $w_a^* = a/30$ $\beta > 0$
S3		LC $\rho < 0$: Dipolar $K < 0$: Quadrupolar	[0.190033, 0.198061]	[0.198061, 0.311203]	$\alpha = 1.0$ $w_a^* = a/15$ $\beta > 0$
S4		LC $\rho < 0$: Quadrupolar $K < 0$: Monopolar+ Quadrupolar	[0.13852, 0.198061]	[0.198061, 0.208064]	$\alpha = 0.5$ $w_a^* = a/30$ $\beta > 0$
S5		LC $\rho < 0$: Quadrupolar $K < 0$: Monopolar+ Quadrupolar	[0.133584, 0.198061]	[0.198061, 0.199365]	$\alpha = 1.0$ $w_a^* = a/30$ $\beta > 0$
S6		LC $\rho < 0$: Quadrupolar $K < 0$: Monopolar+ Quadrupolar	[0.145441, 0.198061]	[0.198061, 0.210904]	$\alpha = 1.5$ $w_a^* = a/30$ $\beta > 0$

S7		LC $\rho < 0$: Quadrupolar $K < 0$: Monopolar+ Quadrupolar	[0.167848, 0.198061]	[0.198061, 0.264008]	$\alpha = 1.0$ $w_a^* = a/15$ $\beta > 0$
S8		LC $\rho < 0$: Dipolar $K < 0$: Quadrupolar	[0.148489, 0.198061]	[0.198061, 0.213618]	$\alpha = 1.0$ $w_a^* = a/30$ $\beta > 0$
S9		LC $\rho < 0$: Dipolar $K < 0$: Quadrupolar	[0.140899, 0.198061]	[0.198061, 0.212211]	$\alpha = 1.5$ $w_a^* = a/30$ $\beta > 0$
S10		LC $\rho < 0$: Dipolar $K < 0$: Quadrupolar	[0.176696, 0.198061]	[0.198061, 0.243152]	$\alpha = 1.0$ $w_a^* = a/15$ $\beta > 0$
S11		Mie $\rho < 0$: Quadrupolar $K < 0$: Monopolar+ Quadrupolar	None	[0.25438, 0.379423]	$\alpha = 0$ $w_a^* = a/15$ $\beta \leq 0$
S12		Mie $\rho < 0$: Quadrupolar $K < 0$: Monopolar+ Quadrupolar	[0.147504, 0.198061]	[0.198061, 0.263384]	$\alpha = 0$ $w_a^* = a/15$ $\beta \leq 0$
S13		Mie $\rho < 0$: Quadrupolar $K < 0$: Monopolar+ Quadrupolar	[0.191479, 0.198061]	[0.198061, 0.354621]	$\alpha = 1.0$ $w_a^* = a/15$ $\beta \leq 0$

S14		Mie $\rho < 0$: Quadrupolar $K < 0$: Monopolar+ Quadrupolar	[0.156749, 0.198061]	[0.198061, 0.280516]	$\alpha = 0$ $w_a^* = a/15$ $\beta \leq 0$ $\Omega^* = 0.09903$
S15		Mie $\rho < 0$: Quadrupolar $K < 0$: Monopolar+ Quadrupolar	[0.146731, 0.198061]	[0.198061, 0.267489]	$\alpha = 0$ $w_a^* = a/15$ $\beta \leq 0$
S16		Mie $\rho < 0$: Quadrupolar $K < 0$: Monopolar+ Quadrupolar	[0.161667, 0.198061]	[0.198061, 0.270861]	$\alpha = 1.0$ $w_a^* = a/15$ $\beta \leq 0$

References

- [1] Pendry, J.B., 2000. Negative refraction makes a perfect lens. *Phys. Rev. Lett.* 85, 3966.
- [2] Fang, N., Xi, D., Xu, J., Ambati, M., Srituravanich, W., Sun, C., Zhang, X., 2006. Ultrasonic metamaterials with negative modulus. *Nat. Mater.* 5, 452.
- [3] Valentine, J., Zhang, S., Zentgraf, T., Ulin-Avila, E., Genov, D. A., Bartal, G., Zhang, X., 2008. Three-dimensional optical metamaterial with a negative refractive index. *Nature* 455, 376.
- [4] Han, T., Bai, X., Thong, J. T., Li, B., Qiu, C. W., 2014. Full control and manipulation of heat signatures: Cloaking, camouflage and thermal metamaterials. *Adv. Mater.* 26, 1731-1734.
- [5] Frenzel, T., Kadic, M., Wegener, M., 2017. Three-dimensional mechanical metamaterials with a twist. *Science*, 358, 1072-1074.
- [6] Matlack, K. H., Serra-Garcia, M., Palermo, A., Huber, S. D., Daraio, C., 2018. Designing perturbative metamaterials from discrete models. *Nat. Mater.* 17, 323-328.
- [7] Liang, Z., Li, J., 2012. Extreme acoustic metamaterial by coiling up space. *Phys. Rev. Lett.* 108, 114301.
- [8] Liu, Z., Zhang, X., Mao, Y., Zhu, Y. Y., Yang, Z., Chan, C. T., Sheng, P., 2000. Locally resonant sonic materials. *Science* 289, 1734-1736.
- [9] Lai, Y., Wu, Y., Sheng, P., Zhang, Z. Q., 2011. Hybrid elastic solids. *Nat. Mater.* 10, 620.
- [10] Zhu, R., Liu, X. N., Hu, G. K., Sun, C. T., Huang, G. L., 2014. Negative refraction of elastic waves at the deep-subwavelength scale in a single-phase metamaterial. *Nat. Commun.* 5, 5510.
- [11] Dong, H. W., Zhao, S. D., Wang, Y. S., Zhang, C., 2017. Topology optimization of anisotropic broadband double-negative elastic metamaterials. *J. Mech. Phys. Solids* 105, 54-80.
- [12] Dong, H. W., Zhao, S. D., Wang, Y. S., Zhang, C., 2018. Broadband single-phase hyperbolic elastic metamaterials for super-resolution imaging. *Sci. Rep.* 8, 2247.
- [13] Lee, S. H., Choi, M., Kim, T. T., Lee, S., Liu, M., Yin, X., Zhang, X., 2012. Switching terahertz waves with gate-controlled active graphene metamaterials. *Nat. Mater.* 11, 936.
- [14] Zhang, X., Liu, Z., 2008. Superlenses to overcome the diffraction limit. *Nat. Mater.* 7(6), 435.

- [15] Kaina, N., Lemoult, F., Fink, M., Lerosey, G., 2015. Negative refractive index and acoustic superlens from multiple scattering in single negative metamaterials. *Nature*, 525, 77.
- [16] Zigoneanu, L., Popa, B. I., Cummer, S. A., 2011. Design and measurements of a broadband two-dimensional acoustic lens. *Phys. Rev. B* 84, 024305.
- [17] Li, Y., Yu, G., Liang, B., Zou, X., Li, G., Cheng, S., Cheng, J., 2014. Three-dimensional ultrathin planar lenses by acoustic metamaterials. *Sci. Rep.* 4, 6830.
- [18] Li, J., Fok, L., Yin, X., Bartal, G., Zhang, X., 2009. Experimental demonstration of an acoustic magnifying hyperlens. *Nat. Mater.* 8, 931.
- [19] Zhu, J., Christensen, J., Jung, J., Martin-Moreno, L., Yin, X., Fok, L., Garcia-Vidal, F. J., 2011. A holey-structured metamaterial for acoustic deep-subwavelength imaging. *Nat. Phys.* 7, 52.
- [20] Park, J. J., Park, C. M., Lee, K. J. B., Lee, S. H., 2015. Acoustic superlens using membrane-based metamaterials. *Appl. Phys. Lett.* 106, 051901.
- [21] Lanoy, M., Pierrat, R., Lemoult, F., Fink, M., Leroy, V., Tourin, A., 2015. Subwavelength focusing in bubbly media using broadband time reversal. *Phys. Rev. B* 91, 224202.
- [22] Molerón, M., Daraio, C., 2015. Acoustic metamaterial for subwavelength edge detection. *Nat. Commun.* 6, 8037.
- [23] Shen, C., Xie, Y., Sui, N., Wang, W., Cummer, S. A., Jing, Y., 2015. Broadband acoustic hyperbolic metamaterial. *Phys. Rev. Lett.* 115, 254301.
- [24] Christensen, J., de Abajo, F.J.G., 2012. Anisotropic metamaterials for full control of acoustic waves. *Phys. Rev. Lett.* 108, 124301.
- [25] Lee, S. H., Park, C. M., Seo, Y. M., Wang, Z. G., Kim, C. K., 2010. Composite acoustic medium with simultaneously negative density and modulus. *Phys. Rev. Lett.* 104, 054301.
- [26] Yang, M., Ma, G., Yang, Z., Sheng, P., 2013. Coupled membranes with doubly negative mass density and bulk modulus. *Phys. Rev. Lett.* 110, 134301.
- [27] Shen, C., Xu, J., Fang, X. N., Jing, Y., 2014. Anisotropic complementary acoustic metamaterial for canceling out aberrating layers. *Phys. Rev. X* 4, 041033.
- [28] Zhou, Y., Fang, X., Li, D., Hao, T., Li, Y., 2018. Acoustic multiband double negativity from coupled single-negative resonators. *Phys. Rev. Appl.* 10, 044006.
- [29] Henríquez, V. C., García-Chocano, V. M., Sánchez-Dehesa, J., 2017. Viscothermal losses in double-negative acoustic metamaterials. *Phys. Rev. Appl.* 8, 014029.
- [30] Brunet, T., Merlin, A., Mascaro, B., Zimny, K., Leng, J., Poncelet, O., Mondain-Monval, O., 2015. Soft 3D acoustic metamaterial with negative index. *Nat. Mater.* 14(4), 384.
- [31] Xie, Y., Wang, W., Chen, H., Konneker, A., Popa, B. I., Cummer, S. A., 2014. Wavefront modulation and subwavelength diffractive acoustics with an acoustic metasurface. *Nat. Commun.* 5, 5553.
- [32] Cummer, S. A., Christensen, J., Alù, A., 2016. Controlling sound with acoustic metamaterials. *Nat. Rev. Mater.* 1, 16001.
- [33] Otomori, M., Yamada, T., Izui, K., Nishiwaki, S., Andkjær, J., 2017. Topology optimization of hyperbolic metamaterials for an optical hyperlens. *Struct. Multidiscip. O.* 55, 913-923.
- [34] Sanchis, L., García-Chocano, V. M., Llopis-Pontiveros, R., Climente, A., Martínez-Pastor, J., Cervera, F., Sánchez-Dehesa, J., 2013. Three-dimensional axisymmetric cloak based on the cancellation of acoustic scattering from a sphere. *Phys. Rev. Lett.* 110, 124301.
- [35] Christiansen, R. E., Sigmund, O., 2016. Designing meta material slabs exhibiting negative refraction using topology optimization. *Struct. Multidiscip. O.* 54, 469-482.
- [36] Yang, X., Kim, Y. Y., 2018. Topology optimization for the design of perfect mode-converting anisotropic elastic metamaterials. *Compos. Struct.* 201, 161-177.
- [37] Wang, F., 2018. Systematic design of 3D auxetic lattice materials with programmable Poisson's ratio for finite strains. *J. Mech. Phys. Solids* 114, 303-318.
- [38] Chen, Y., Meng, F., Li, G., Huang, X., 2018. Topology optimization of photonic crystals with exotic properties resulting from Dirac-like cones. *Acta Mater.*, 164, 377-389.

- [39] Li, D., Zigoneanu, L., Popa, B. I., Cummer, S. A., 2012. Design of an acoustic metamaterial lens using genetic algorithms. *J. Acoust. Soc. Am.* 132, 2823-2833.
- [40] Lu, L., Yamamoto, T., Otomori, M., Yamada, T., Izui, K., Nishiwaki, S., 2013. Topology optimization of an acoustic metamaterial with negative bulk modulus using local resonance. *Finite Elem. Anal. Des.* 72, 1-12.
- [41] Li, E., He, Z. C., Hu, J. Y., Long, X. Y., 2017. Volumetric locking issue with uncertainty in the design of locally resonant acoustic metamaterials. *Comput. Method Appl. M.*, 324, 128-148.
- [42] Goffaux, C., Vigneron, J. P., 2001. Theoretical study of a tunable phononic band gap system. *Phys. Rev. B* 64, 075118.
- [43] Fokin, V., Ambati, M., Sun, C., Zhang, X., 2007. Method for retrieving effective properties of locally resonant acoustic metamaterials. *Phys. Rev. B* 76, 144302.
- [44] Song, B. H., Bolton, J. S., 2000. A transfer-matrix approach for estimating the characteristic impedance and wave numbers of limp and rigid porous materials. *J. Acoust. Soc. Am.* 107, 1131-1152.
- [45] Popa, B. I., Cummer, S. A., 2009. Design and characterization of broadband acoustic composite metamaterials. *Phys. Rev. B* 80, 174303.
- [46] Xie, Y., Popa, B. I., Zigoneanu, L., Cummer, S. A., 2013. Measurement of a broadband negative index with space-coiling acoustic metamaterials. *Phys. Rev. Lett.* 110, 175501.
- [47] Cheng, Y., Zhou, C., Yuan, B. G., Wu, D. J., Wei, Q., Liu, X. J., 2015. Ultra-sparse metasurface for high reflection of low-frequency sound based on artificial Mie resonances. *Nat. Mater.* 14, 1013.
- [48] Graciá-Salgado, R., García-Chocano, V. M., Torrent, D., Sánchez-Dehesa, J., 2013. Negative mass density and ρ -near-zero quasi-two-dimensional metamaterials: Design and applications. *Phys. Rev. B* 88(22), 224305.
- [49] Zhou, S., Li, W., Chen, Y., Sun, G., Li, Q., 2011. Topology optimization for negative permeability metamaterials using level-set algorithm. *Acta Mater.* 59(7), 2624-2636.
- [50] Guo, X., Zhang, W., Zhong, W., 2014. Doing topology optimization explicitly and geometrically—a new moving morphable components based framework. *J. Appl. Mech.* 81(8), 081009.
- [51] Aage, N., Andreassen, E., Lazarov, B. S., Sigmund, O., 2017. Giga-voxel computational morphogenesis for structural design. *Nature* 550, 84.
- [52] Zhang, X., He, J., Takezawa, A., Kang, Z., 2018. Robust topology optimization of phononic crystals with random field uncertainty. *Int. J. Numer. Methods Eng.*, 1-20.
- [53] Dong, H. W., Su, X. X., Wang, Y. S., Zhang, C., 2014. Topological optimization of two-dimensional phononic crystals based on the finite element method and genetic algorithm. *Struct. Multidiscip. O.* 50, 593-604.
- [54] Dong, H. W., Su, X. X., Wang, Y. S., 2014. Multi-objective optimization of two-dimensional porous phononic crystals. *J. Phys. D Appl. Phys.* 47(15), 155301.
- [55] Shen, C., Xie, Y., Li, J., Cummer, S. A., Jing, Y., 2016. Asymmetric acoustic transmission through near-zero-index and gradient-index metasurfaces. *Appl. Phys. Lett.* 108, 223502.
- [56] Ward, G. P., Lovelock, R. K., Murray, A. R. J., Hibbins, A. P., Sambles, J. R., Smith, J. D., 2015. Boundary-layer effects on acoustic transmission through narrow slit cavities. *Phys. Rev. Lett.* 115, 044302.
- [57] Molerón, M., Serra-Garcia, M., Daraio, C., 2016. Visco-thermal effects in acoustic metamaterials: from total transmission to total reflection and high absorption. *New J. Phys.* 18, 033003.
- [58] Gerard, N. J., Li, Y., Jing, Y., 2018. Investigation of acoustic metasurfaces with constituent material properties considered. *J. Appl. Phys.* 123, 124905.